



HAL
open science

Influence of electrode material and roughness on iron electrodeposits dispersion by ultrasonification

Audrey Iranzo, Fabien Chauvet, Théodore Tzedakis

► **To cite this version:**

Audrey Iranzo, Fabien Chauvet, Théodore Tzedakis. Influence of electrode material and roughness on iron electrodeposits dispersion by ultrasonification. *Electrochimica Acta*, 2015, vol. 184, pp. 436-451. 10.1016/j.electacta.2015.10.052 . hal-01278898

HAL Id: hal-01278898

<https://hal.science/hal-01278898>

Submitted on 25 Feb 2016

HAL is a multi-disciplinary open access archive for the deposit and dissemination of scientific research documents, whether they are published or not. The documents may come from teaching and research institutions in France or abroad, or from public or private research centers.

L'archive ouverte pluridisciplinaire **HAL**, est destinée au dépôt et à la diffusion de documents scientifiques de niveau recherche, publiés ou non, émanant des établissements d'enseignement et de recherche français ou étrangers, des laboratoires publics ou privés.



Open Archive TOULOUSE Archive Ouverte (OATAO)

OATAO is an open access repository that collects the work of Toulouse researchers and makes it freely available over the web where possible.

This is an author-deposited version published in : <http://oatao.univ-toulouse.fr/>
Eprints ID : 15089

To link to this article : DOI:10.1016/j.electacta.2015.10.052
URL : <http://dx.doi.org/10.1016/j.electacta.2015.10.052>

To cite this version : Iranzo, Audrey and Chauvet, Fabien and Tzedakis, Théodore *Influence of electrode material and roughness on iron electrodeposits dispersion by ultrasonification*. (2015) *Electrochimica Acta*, vol. 184. pp. 436-451. ISSN [0013-4686](#)

Any correspondence concerning this service should be sent to the repository administrator: staff-oatao@listes-diff.inp-toulouse.fr

Influence of electrode material and roughness on iron electrodeposits dispersion by ultrasonification

A. Iranzo^{a,b}, F. Chauvet^{a,b,*}, T. Tzedakis^{a,b,**}

^a Université de Toulouse, INPT, UPS, Laboratoire de Génie Chimique, 118 Route de Narbonne, F-31062 Toulouse, France

^b CNRS, UMR 5503, F-31062 Toulouse, France

ABSTRACT

This study relates the sonoelectrochemical production of metallic particles and nanoparticles. The emphasis is on the influence of electrode material and roughness on the morphology of iron electrodeposits and their dispersion from the electrode by ultrasonification. Ultrasonification is either applied during cyclic voltammetries with solution stirring or after galvanostatic iron electrodeposition; no dispersion was observed when using a gold electrode, whereas dispersion was always observed when using vitreous carbon (VC) substrates. Scanning Electron Microscopy (SEM) imaging of the electrodeposits shows higher iron coverage on gold than on VC electrodes. Iron spreads more on gold than on VC. The values of both the interfacial energy of the iron/electrode interface and the work of adhesion of iron on the electrode are in agreement with the previous observations. Dispersion kinetics on VC were found to be dependent on the electrode surface roughness. Results suggest that dispersion follows a first order kinetics, which is coherent with the constant action of cavitation bubbles in the vicinity of the electrode surface. Enhancement of mass-transfer by ultrasound has also been observed.

Keywords:

zero-valent iron electrodeposition
sonoelectrochemistry
adhesion energy
surface roughness
electrodeposits dispersion

1. Introduction

Iron-based nanoparticles (Fe_3O_4 , $\gamma\text{-Fe}_3\text{O}_4$, nickel-cobalt-iron alloy) exhibit interesting magnetic properties in the medical field, such as contrast agents for Magnetic Resonance Imaging [1,2] and for treatment of tumors by hyperthermia [3,2]. Recent studies [4] indicate that zero-valent iron nanoparticles (ZVI-nP) show better magnetic performance than iron oxides for medical applications. ZVI-nP can also be used for various other applications such as an effective reducing agent: i) in water treatment [5], ii) for dechlorination [6,7], iii) nitrate removal [7–9], and iv) for destruction of various other pollutants (see [5] for an extensive review).

ZVI-nP can be synthesized by several techniques (see [10] and [5] for an exhaustive list): ball milling [11], thermal reduction (reduction of iron salts [12] and reduction of oxide [13]), iron salts wet-chemical reduction [6,14] (using borohydride salt as a

reducing agent) and direct electrochemical reduction [15,16,9]. The most widely used technique is the wet-chemical method.

Scaling-up of wet-chemical method, in order to produce large quantities of ZVI-nP, requires expensive reagents and specific security conditions because of the gaseous hydrogen production [12].

Direct electrochemical ZVI-nP synthesis appears as a promising technique for economic and safe production processes, especially at a large scale; the reducing reagent is replaced by electricity and under controlled conditions hydrogen production is avoided. Nevertheless, metallic iron, produced at the cathodic surface, must be removed from the electrode and dispersed in the liquid at the required size. Various works involve ultrasonic dispersion of electrodeposited iron, simultaneously or sequentially with iron-precursors reduction, allowing the renewal of the cathode surface. Generally, power ultrasounds (~ 20 kHz, using an ultrasonic horn or bath) are used to generate cavitation bubbles that, during their violent collapses, create fluid motion which removes solid deposits from the electrode surface. During iron electrodeposition, under sequential pulses of the applied current, Delplancke et al. [15] apply shifted pulses of ultrasounds, using a titanium ultrasonic horn (20 kHz, 50 W/cm^2), also used as the polarized cathode. Nanoparticles (6 nm – 100 nm) of pure Fe and alloys of Fe/Ni/Co have been successfully synthesized in aqueous solutions; partial ‘chemical oxidation’ of pure iron particles has been observed. In

* Corresponding author at: Laboratoire de Génie Chimique, UMR CNRS 5503, Université de Toulouse III-PS, INPT, 118 route de Narbonne, F-31062 Toulouse, France. Tel.: +33561557468.

** Corresponding author at: Laboratoire de Génie Chimique, UMR CNRS 5503, Université de Toulouse III-PS, INPT, 118 route de Narbonne, F-31062 Toulouse, France. Tel.: +33561558302.

E-mail addresses: chauvet@chimie.ups-tlse.fr (F. Chauvet), tzedakis@chimie.ups-tlse.fr (T. Tzedakis).

Nomenclature

A	geometric surface area (m^2)
A_{elect}	Hamaker constant of electrode material, <i>elect</i> = Au or VC (J)
$A_{elect/L/Fe}$	Hamaker constant for electrode material (<i>elect</i> = Au or VC) and iron interacting across the liquid (J)
Ar	Argon
A_{Fe}, A_L	Hamaker constants of the iron and the liquid (J)
C_{H^+}	Protons concentration (mol/m^3)
d	Separation distance (m)
D	Diffusion coefficient (m^2/s)
e	Thickness of the deposit (m)
E_{adh}	Adhesion energy of iron on VC electrode = $W_{Fe/VC}S_{Fe/VC}$ (J)
E	Electrode potential (V)
F	Faraday constant (96,500 C/mol)
h	Local surface height (m)
j_{lim}	Limiting current density (A/m^2)
$I, I_{applied}, I_{lim}$	Current, applied current and limiting current (A)
M_{Fe}	Molecular weight of iron (kg/mol)
n	Electrons number
$Q_c, Q_a,$ and $Q_{a_{ref}}$	Respectively the cathodic, the anodic and the anodic reference amount of charges (C)
r	Potential scan rate (mV/s)
r_a	Arithmetic roughness (m)
r_w	Wenzel's roughness = ratio between actual surface and geometrical surface
s	Dispersion rate constant (s^{-1})
S_{disk}	Surface area of the disk electrode (m^2)
t	Time (s)
t_{US}	Ultrasonication duration (s)
$W_{Fe/elect}$	Work of adhesion of iron on the electrode, <i>elect</i> = Au or VC (J/m^2)
x, y	Cartesian coordinates (m)
Greek letters	
γ_a	Surface tension of medium a (J/m^2)
$\gamma_{a/b}$	Interfacial tension between both media a and b (J/m^2)
γ_{elect}	Surface energy of the electrode, <i>elect</i> = Au or VC1 or VC2 (J/m^2)
γ_d and γ_p	Respectively the dispersive and the polar components of the surface energy (J/m^2)
η	Overpotential (V)
ρ_{Fe}	Volumetric mass of iron (kg/m^3)
ν	Kinematic viscosity (m^2/s)
$\Phi_{a/b}$	Adjustment parameter which depends on interactions between both interacting media a and b
ω	Angular velocity (rpm)

another study [16], cathode is assembled both with a high (0.2–2 MHz, 5 W/cm²) and a low (20 kHz, 100 W/cm²) frequency ultrasonic transducers who irradiate the cathodic area; constant current electrolyses were carried out in tetrahydrofuran, under ultrasonication, and 10 nm sized ZVI-nP are produced when the low and the high frequency transducers are used simultaneously. Chen et al. [9], claim that ZVI-nP ranging between 1–20 nm were synthesized using aqueous 1 M FeCl₃ in the presence of

cetylpyridinium chloride as a dispersing agent; a two platinum electrodes 'classical electrochemical cell', 'entirely' immersed into an ultrasonic bath (20 kHz), was used and galvanostatic electrolyses were carried out under ultrasonication. Other metallic nanoparticles (silver, palladium, platinum, zinc, nickel, gold) have been synthesized by the sonoelectrochemical method, see [17] for a review. Previous studies were generally devoted to determining the best operating parameters (pulse times, current, temperature, ultrasounds intensity, stabilizers, etc.) for a given set-up allowing the synthesis of desired nanoparticles.

Effects of power ultrasound on various electrochemical systems have also been extensively studied. Ultrasounds are generally applied using a titanium ultrasonic horn acting as the ultrasound generator placed in front of the working electrode ('face-on' configuration); the working electrode can also be directly integrated on the ultrasonic horn ([18]). Another possibility is to immerse the electrochemical cell in an ultrasonic bath [19]. Among other effects and regardless of the experimental configuration, ultrasounds induce cavitation bubbles and acoustic streaming which enhance mass-transfer leading to an increase of the current [20–25,19]. Current fluctuations are also observed due to violent bubble collapses [21,26,27].

The ability of the fluid motion and also the shocks induced by ultrasound to 'clean' the electrode surface has been investigated in several works. Cavitation bubble collapses induced by ultrasound were found to be able to activate electrodes avoiding passivation by 'eroding/roughening' the electrode material [28,19]. Coupling mercury electrodeposition and ultrasonication simultaneously on a vitreous carbon electrode has led to a 'steady state' regime where the quantity of electrodeposited Hg on the electrode remains constant (electrodeposition flux = ablation flux) [29]. Under ultrasonication, the electrodeposition of metals such as Zn, Co, Pb, and Hg, was investigated on a vitreous carbon substrate by cyclic voltammetry in [30] (see also [31]). The authors analyzed the ratio of anodic to cathodic charges as a function of the ultrasound intensity, for their particular experimental conditions (potential scan rate, sonoelectrochemical system, electrode material . . .), and showed that it depends on both the ultrasound intensity and the metal used. This suggests the importance of metal/substrate affinity on the electrodeposits dispersion. Considering the case of a particle lying on a substrate and submitted to ultrasonication in [32], the authors discussed the competition between the hydrodynamic forces and the adhesion force as a function of the particle size; they showed that ultrasounds should be able to remove submicrometer particles but not smaller particles such as molecular adsorbates (adhesion outweighs hydrodynamics forces).

These previous studies show that the efficiency of ultrasound to remove/disperse electrodeposited metals should depend on:

- the ultrasound intensity (and the experimental configuration used) [30,31]
- the size/morphology and the spatial distribution of deposited metallic particles [32]
- the adhesion energy of electrodeposited metal on the electrode material

Note that, to date, the effect of the adhesion energy of the electrodeposited metal on the electrode substrate, has not been directly investigated.

In the present work, the dispersion by ultrasound of iron electrodeposits is studied for various electrode materials (gold and vitreous carbons) which allows to vary the adhesion energy. The effect of the electrode material on the morphology of the electrodeposited iron is also studied by SEM imaging. The influence of the electrode surface roughness is investigated using VC electrodes having different levels of polishing.

The study is based on the analysis of electrochemical measurements: voltamperometries and galvanostatic electrolyses coupled simultaneously or sequentially with ultrasonification. Experiments were realized in a classical electrochemical cell immersed in an ultrasonic bath. Two different salts (FeCl_2 and $(\text{NH}_4)_2\text{Fe}(\text{SO}_4)_2$) were used as iron electrodeposit precursors.

Experimental results on iron electrodeposits morphology and adhesion are discussed on the basis of a theoretical analysis, enabling the estimation of the work of adhesion and the interfacial tension between iron and the substrate, which is presented in the [Appendix](#).

2. Material and methods

2.1. Chemicals and experimental set-up

All solutions, prepared using ultrapure water (18.2 M Ω .cm), were deaerated before experiments (Argon, 1 bar), for a duration of at least 15 min; argon sparging during the experiments which were achieved at room temperature ($18 < T(^{\circ}\text{C}) < 22$), except for experiments under ultrasonic irradiation, for which the temperature slightly increases ($\Delta T < 5^{\circ}\text{C}$). Solutions containing 0.01 M of iron (II) were prepared by dissolving Normapur solid FeCl_2 or $(\text{NH}_4)_2\text{Fe}(\text{SO}_4)_2$ (Mohr's salt) supplied by Sigma-Aldrich. Solutions also contain respectively 0.1 M KCl or 0.05 M K_2SO_4 as supporting electrolytes, and their pH was adjusted to 4.0, using HCl or H_2SO_4 respectively.

The iron (II) was preferred to iron (III) in order to avoid the oxidation of electrodeposited iron by the latter. Moreover, using two different counter-ions (chloride or sulfate) allows to study their effect on the morphology of the electrodeposited iron.

FeCl_2 was selected because it is a simple, soluble and cheap iron (II) salt; it has already been used to study iron nucleation on vitreous carbon in [33]. Furthermore, another work [9] has shown that iron nanoparticles could be synthesized by sonoelectrochemistry using FeCl_3 .

$(\text{NH}_4)_2\text{Fe}(\text{SO}_4)_2$ complex, preferred to the simple salt $\text{Fe}(\text{SO}_4)_2$, was also studied thanks to its 'chemical stability' against to the oxidation by oxygen.

Electrochemical experiments were performed in a classical three electrodes cell (50 mL), either by cyclic voltammetric scans or by galvanostatic electrolyses; a rotating disk was used as a working electrode (Radiometer, EDI101T), a platinum foil constitutes the counter electrode, and a saturated calomel electrode (SCE) immersed within a Luggin capillary is the reference electrode.

Solution was always stirred by the rotation of the disk electrode (angular velocity $\omega = 1000$ rpm). For cyclic voltammetry, the potential scan rate r is equal to 20 mV/s except for particular cases where lower scan rates were used. For galvanostatic electrolyses, the applied current is equal to 90% of the limiting current corresponding to $\text{Fe}^{(II)}$ reduction which is measured on cyclic voltammetry scans (without ultrasound).

Depending on the experiment, the electrochemical cell was immersed in an ultrasonic bath (Fisher Scientific FB 15057, 37 kHz, 750 W, 6.9 L). A potentiostat Voltalab PGZ 100 from Radiometer-Analytical is used to achieve the electrochemical measurements. Voltmaster 4 is the electrochemical software used to control the potentiostat. Working electrode material is either gold (2 mm diameter, purity > 99.99%) or vitreous carbon 1 (VC1, 3 mm diameter, purity = 99.96%) or vitreous carbon 2 (VC2, 3 mm diameter, purity = 99.99%). VC1 was provided by Carbone Lorraine Company and VC2 was provided by Origalys Company. Chemical composition of these VC electrodes are slightly different: 0.04% ash content and 50 ppm sulfur and bore traces for VC1, 0.0042% ash content and 13.5 ppm metal traces for VC2 (data provided by suppliers). The main difference between VC1 and VC2 is that VC1 has fabrication defects (small void inclusions in its volume) and thus its surface exhibits

holes with diameters of about 1-10 μm (even after polishing at 0.3 μm), while the VC2 has no defects. VC1 and VC2 surfaces characterization is given in section 3.3 where the effect of electrode surface roughness on electrodeposit adhesion is discussed.

Electrodes were polished using alumina aqueous suspension of 9, 5, 1 and 0.3 μm on a rotating pad. The electrodes were sonicated for 5 minutes in a 50:50 ethanol/water mixture between each polishing and 5 minutes more in ultrapure water to remove remaining alumina particles.

2.2. Electrode surface characterization

The surfaces of the electrodes were visualized by an optical microscope (Zeiss Axiolab) and surface profiles were measured by an interferometric surface profiler (Zygo 3D). Using data provided by Zygo 3D measurements, Wenzel's roughness r_w (defined as the ratio between actual surface and geometrical surface) can be estimated using the following equation:

$$r_w = \frac{1}{A} \int_A \sqrt{1 + \nabla h(x,y)^2} dx dy \quad (1)$$

where A is the geometric surface area, h is the local surface height and x, y are the Cartesian coordinates. r_w was computed using a home-made Matlab program. Arithmetic surface roughness r_a was computed by the Zygo software.

2.3. Measurement of surface energies of electrodes

Electrode surface energy or surface tension γ_{elect} ($elect = \text{Au}$ or VC1 or VC2) is an important parameter allowing the estimation of both the work of adhesion of metallic iron on the electrode material in electrolytic solution $W_{\text{Fe}/elect}$ and also the interfacial tension between the electrode and the iron $\gamma_{\text{Fe}/elect}$. The surface tensions of the gold and VC electrodes, γ_{Au} , γ_{VC1} and γ_{VC2} , were obtained by measuring the contact angles of a series of liquids of known surface tensions directly on the polished electrodes surfaces (Owens-Wendt 'one liquid method' [34]). Contact angles of ultrapure water, glycerol, dimethylsulfoxide and decane were measured with a GBX Digidrop goniometer DGD fast/60 using $\sim 2 \mu\text{L}$ liquid droplet in ambient conditions. The measurement of contact angles was reproducible in the range $\pm 5^{\circ}$. Absolute uncertainty on γ_{elect} measurement is lower than 4 mJ/m 2 .

2.4. Electrodeposit morphology analysis

Morphology of iron electrodeposits was observed by SEM with a MEB FEG JEOL JSM 7100F TTLS or a MEB FEG JEOL JSM 7800F Prime-EDS. Before observation, the sample was rinsed with ultrapure water (to avoid electrolyte crystallization) and dried under ambient conditions. To avoid electrons beam deviation (due to the presence of insulating material surrounding the disk electrode), the whole sample surface was coated by a nanometric layer of gold by vapor deposition, if required. An electric connection between electrodes and the SEM support was insured by a brass stud adapted to the electrode.

3. Results and discussion

3.1. Iron electrodeposition by cyclic scan voltammetry under silent conditions

3.1.1. $\text{Fe}^{(II)}$ electrochemical behaviour on gold and vitreous carbon electrodes

The electrochemical behavior of $\text{Fe}^{(II)}$ salts used (FeCl_2 and Mohr's salt) were examined in presence of two supporting

electrolytes and on three different electrodes polished with the finest alumina suspension (0.3 μm): VC1, VC2 and gold. Voltamperometric curves obtained (under stirring) without $\text{Fe}^{(II)}$ (residual

currents, see insets in Fig. 1 a and b) reveal a diffusion-limited wave attributed to the reduction of the free protons at $\text{pH} = 4$:

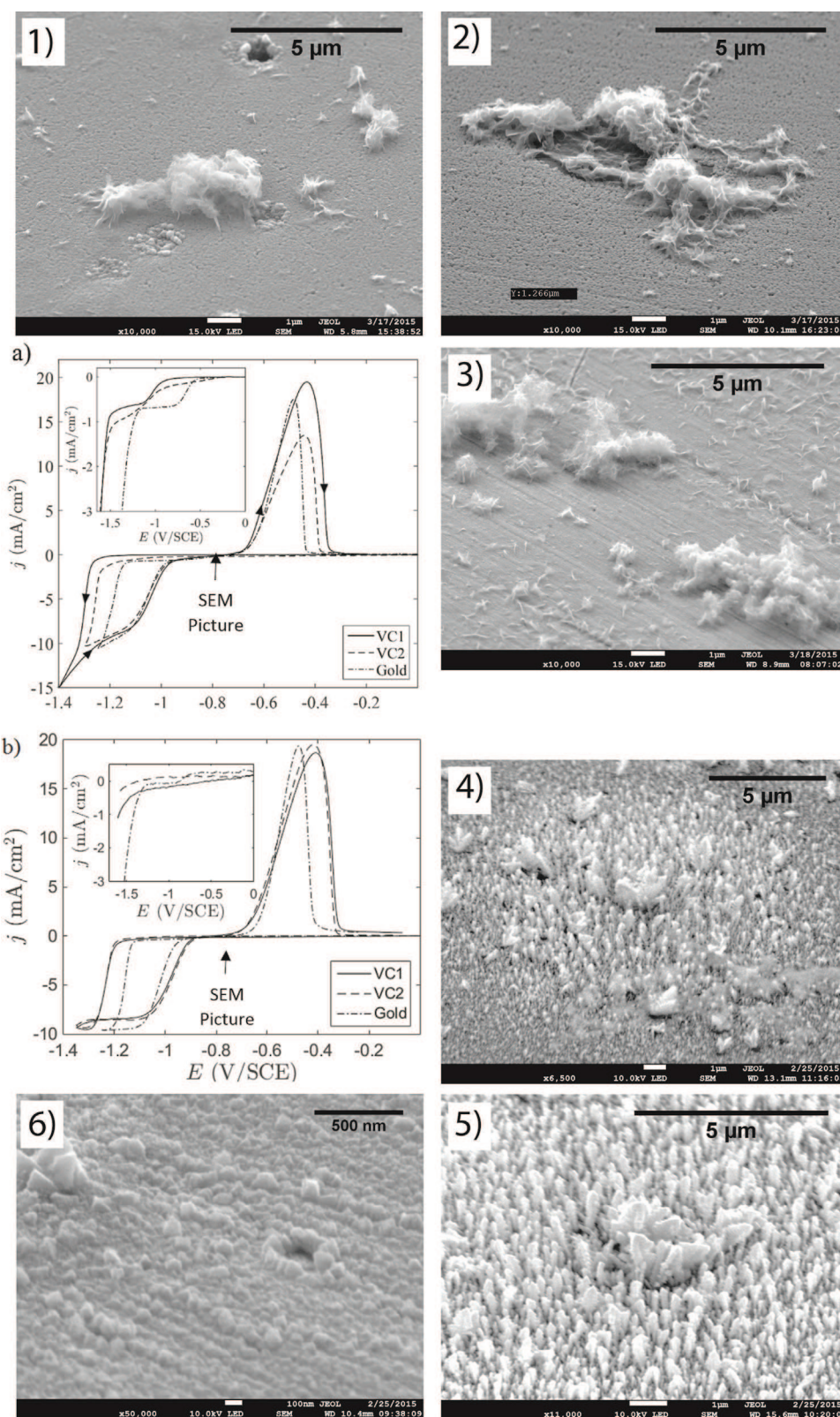


Fig. 1. Cyclic voltammograms scans and the corresponding SEM pictures. a) and b): curves (forward and backward, see arrows in a)) obtained on a rotating disk electrode for three different materials: VC1, VC2 and gold. a): Mohr's salt solution, b): FeCl_2 solution. **Insets:** Residual currents (forward curves). **SEM pictures** (taken at the end of the cathodic cycle, see the arrow on a) and b)); 1) to 3) iron electrodeposits using Mohr's salt solution on respectively VC1, VC2 and gold electrodes; 4) to 6) iron electrodeposits using FeCl_2 solution on respectively VC1, VC2 and gold electrodes.



Curves obtained with the electrolyte K_2SO_4 alone (inset in Fig. 1a) exhibit a resolute diffusion-limited wave, of which the limiting current, even low magnitude (0.65 mA/cm^2), appears to be constant for the three examined materials (same hydrodynamics). Concerning the curve obtained in presence of KCl (inset in Fig. 1b), it does not show a clear signal for the H^+ reduction before the reduction of water ($2\text{H}_2\text{O} + 2\text{e}^- \rightarrow \text{H}_2 + 2\text{OH}^-$), except for the gold cathode. Indeed the H^+ reduction on the VC is not visible (see inset in Fig. 1b) because it is shifted to more negative potentials and screened by water reduction. This phenomenon has already been observed by Grujicic and Pestic ([33]) who studied iron electrodeposition from sulfate and chloride solutions on VC. Moreover, for the gold cathode, the corresponding limiting current (0.34 mA/cm^2) is half of the magnitude of sulfate system ones (0.68 mA/cm^2). This ratio of 2 between these limiting current values is attributed to the di-acid nature of H_2SO_4 compared to the mono-acid nature of HCl. Indeed, a solution of sulfuric acid and K_2SO_4 at $\text{pH}=4$ contains the following species: H^+ , HSO_4^- , SO_4^{2-} and K^+ , so after the consumption of the free H^+ , HSO_4^- dissociates and supply additional H^+ which could be reduced. This leads, for the sulfate system, to an apparent H^+ concentration two times higher than the one for the chloride system, and explains why a limiting current (which is proportional to concentration) that is two times higher has been measured for the sulfate system.

Values for limiting current density, j_{lim} , can be estimated using Levich's equation ([35]):

$$j_{lim} = 0.62 \cdot n \cdot F \cdot D^{2/3} \cdot \nu^{-1/6} \cdot C_{\text{H}^+} \cdot \omega^{1/2}, \quad (3)$$

where n , F , D , ν , C_{H^+} and ω are respectively the electrons number, the Faraday constant, the diffusion coefficient, the kinematic viscosity, the protons concentration and the angular velocity.

Taking the values for D , C_{H^+} , and ν of respectively $9.3 \times 10^{-9} \text{ m}^2/\text{s}$ ([36]), 10^{-4} M and $10^{-6} \text{ m}^2/\text{s}$ leads to $j_{lim} = 0.33 \text{ mA/cm}^2$ which is in accordance with the measured value of j_{lim} for the chloride system (0.34 mA/cm^2 , $C_{\text{H}^+} = 10^{-4} \text{ M}$).

In the presence of iron salts (Fig. 1a and b), all curves (1000 rpm, 20 mV/s) exhibit an additional signal attributed to the $\text{Fe}^{(II)}$ reduction:



For all examined electrode materials (gold, VC1 and VC2), the first scan (starting at $+0.2 \text{ V/SCE}$ toward cathodic potentials) clearly indicates a slow redox system, reductions of $\text{Fe}^{(II)}$ to Fe starting at around -1.2 to -1.3 V/SCE on the initially bare electrodes. During the first scan, vitreous carbons and gold are partially covered by zero-valent iron, so once the switching potential is reached, substrates

tend to act as an iron electrode. Indeed at the potential scan rate used, cathodic curves obtained during the return scan (-1.4 to -0.4 V/SCE), exhibit a resolute diffusion-limited wave, corresponding to the $\text{Fe}^{(II)}$ reductions on the native iron surface. It can be noticed that for Mohr's salt solutions (Fig. 1a), the diffusion-limited wave (pseudo-plateau) is not well defined due to the co-reduction of free protons on electrodeposited iron followed by water reduction. This distinction between chloride and sulfate systems for iron electrodeposition has already been observed by Grujicic and Pestic ([33]).

For the backward scans, the cathodic current was canceled at the equilibrium potentials which lie in the range [~ -0.9 to $\sim -0.8 \text{ V/SCE}$] for the KCl medium and [~ -1 to $\sim -0.9 \text{ V/SCE}$] for the K_2SO_4 medium. These potentials remain relatively far from the Fe^{2+}/Fe Nernst's potential $E = -0.44 - 0.25 + 0.03 \times (\log(10^{-2}/1)) = -0.74 \text{ V/SCE}$. This could be explained by the following reasons:

- the $\text{Fe}^{(II)}$ ions complexed with chloride or by ammonium/sulfate ions (Mohr's salt), so the redox system involved is different from the simple Fe^{2+}/Fe system
- co-reduction of free H^+ (even at the equilibrium potential) disturbs the redox potential of the Fe^{2+}/Fe system due to the increase of the pH at the cathode.

The anodic curves obtained during the backward scan for potentials higher than -0.8 V/SCE , exhibit peaks attributed to the iron electrodeposit oxidation (for both KCl and K_2SO_4 media and for the three substrates, Fig. 1a and 1b):



The sharp decrease in current, clearly indicates complete oxidation of the electrodeposit and the regeneration of the initially bare surface of the working electrode (gold, VC1 and VC2). This is the end of one complete cycle of the operated experiments.

3.1.2. Influence of electrode material on iron electrodeposit morphology

Iron electrodeposits, obtained on the three substrates and for both chloride and sulfate media, were observed by SEM at the end of the cathodic cycle. The resulting pictures are shown in Fig. 1, pictures 1–6.

In chloride medium, a clear morphological difference can be noticed between iron electrodeposits obtained on gold and on vitreous carbon electrodes (Fig. 1, pictures 4–6). Indeed, on the gold electrode (Fig. 1, picture 6), the SEM image reveals iron electrodeposit as a compact layer that covers well the electrode surface. This layer consists of cubic structures sized in the range of a few hundred nanometers. Conversely, on the VC substrates (Fig. 1,

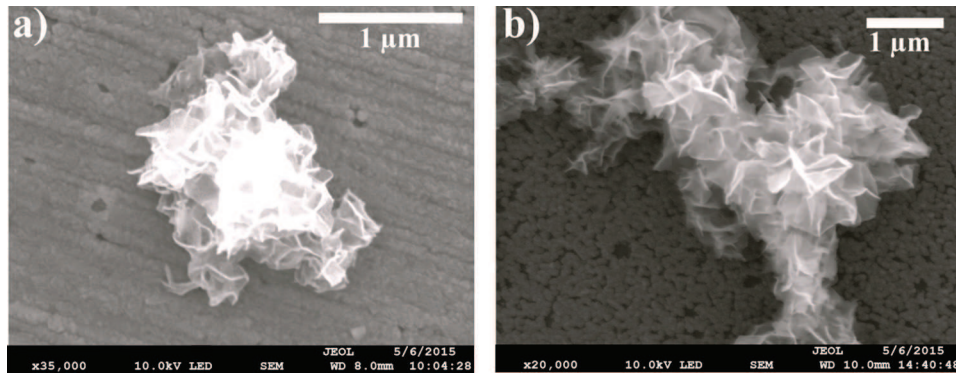


Fig. 2. SEM pictures of iron electrodeposits formed after a cathodic cycle by voltamperometry (starting at 0.2 V/SCE , reversed at -1.3 V/SCE , stopped at -0.8 V/SCE) using Mohr's salt solution for the gold electrode a) and for the VC2 electrode b) respectively.

pictures 4 and 5) iron electrodeposits appear as small micrometric dendritic structures with heights not exceeding 1 μm .

In Mohr's salt medium, iron electrodeposited on gold (Fig. 1, picture 3) and on VC substrates (Fig. 1, pictures 1–2) present quite similar morphology with a thin layer of iron covering the surface (verified by Energy Dispersive X-Ray Spectroscopy) with iron micrometric structures on it. However, a more detailed analysis of this thin layer of iron (Fig. 2) shows that it covers more on the gold electrode (Fig. 2a) than on the VC2 electrode (Fig. 2b). Indeed, on the VC2 electrode, the thin layer of iron is not continuous, some holes (dark spots) are visible revealing the VC substrate through them. On contrary, on the gold substrate, this layer is far more continuous.

Iron electrodeposit morphology depends on the $\text{Fe}^{(II)}$ salt and the solution composition as well as the electrode material. It has been shown that specific counter-ions adsorption could influence electrodeposit morphology ([37]). Here, we focus on the effect of the electrode material on the iron electrodeposit morphology, and our observations show that electrodeposited iron has more affinity with gold than with vitreous carbon electrodes. Iron spreads better on gold than on VC during its electrodeposition for both media used. It has to be noticed that no difference is observed between electrodeposits on VC1 and those on VC2.

From the electrodeposition theory ([38]), it is shown that the growth mode (from 2D to 3D) of a crystal strongly depends on the interfacial energy of interface between the electrodeposit and the electrode $\gamma_{\text{Fe}/\text{elect}}$ (with *elect* corresponding either to *Au* electrode or to *VC* electrodes). Crystals obtained for low values of $\gamma_{\text{Fe}/\text{elect}}$ are almost flat (2D growth) and conversely crystals grow preferentially perpendicularly to the electrode surface (leading to poorly covered electrode surface) for high values of $\gamma_{\text{Fe}/\text{elect}}$ (3D growth).

Contact angle measurements were achieved for gold and VC substrates, see Table 1. Using a theoretical development, the difference between $\gamma_{\text{Fe}/\text{VC}}$ and $\gamma_{\text{Fe}/\text{Au}}$ can be estimated from the measurements of surface energies (see the Appendix). A positive and non-negligible value lying in the range [205.4 mJ/m^2 ; 58.9 mJ/m^2] was deduced for $\gamma_{\text{Fe}/\text{VC}} - \gamma_{\text{Fe}/\text{Au}}$ which is in accordance with the morphological observations of iron electrodeposits.

Voltamperometric curves indicated in Fig. 1a) and 1b), show that the overpotentials η required for iron reduction on the initially bare gold electrode (the first forward scan) η_{Au} are systematically lower than $\eta_{\text{VC1}} \sim \eta_{\text{VC2}}$ for both media used. Therefore, a lower energy (lower cell voltage) is required to create/increase the Fe/Au interface than the Fe/VC interface. This is in accordance with the previous analysis showing that a higher energy is required to increase the surface area of the Fe/VC interface than to increase the one of the Fe/Au interface during iron electrodeposition ($\gamma_{\text{Fe}/\text{VC}} > \gamma_{\text{Fe}/\text{Au}}$).

To conclude, during a cathodic cycle on VC electrodes, iron electrodeposits begin to grow following a 3D mode, leading rapidly to a dendritic growth. On the gold electrode, iron electrodeposits begin to grow following a 2D mode (thin film growth) which delays the appearance of the dendritic growth mode as it is clearly visible in the case of chloride medium (Fig. 1, pictures 4–6).

Table 1

Surface energies of VC1 and VC2 electrodes. γ_d and γ_p are respectively the dispersive and the polar components of the total surface energy $\gamma_{\text{elect}} = \gamma_d + \gamma_p$.

	γ_d (mJ/m^2)	γ_p (mJ/m^2)	γ_{elect} (mJ/m^2)
VC1	19 \pm 2	10 \pm 2	29 \pm 2
VC2	21 \pm 1	12 \pm 2	34 \pm 4

3.1.3. Influence of iron electrodeposit morphology on limiting current of $\text{Fe}^{(II)}$ reduction

The differences in iron electrodeposit morphologies, as discussed above, can be revealed by a detailed analysis of the voltamperograms for both media (chloride and sulfate).

In chloride medium, the great difference in iron morphology observed for gold and VC electrodes (see Fig. 1, pictures 4–6) explains the slight, but systematic difference of limiting current values, measured for both substrates (cathodic backward scan, Fig. 1b). As previously mentioned, on the gold electrode, the SEM image reveals quasi total coverage of the electrode surface by a thin iron layer. Therefore, the electroactive surface area for the gold disk can be considered as the geometrical surface area (see a schematic representation of the electrodeposits in Fig. 3a for gold and 3b for VC). Conversely, on the VC electrodes (Fig. 1, pictures 4 and 5) iron electrodeposits consist of relatively small dendrites of which heights ($< 1 \mu\text{m}$) are lower than the thickness of the diffusion boundary layer thickness (estimated at $\sim 14 \mu\text{m}$). For the VC electrodes case, electroactive surface area is limited to the sum of surface areas of the growing dendrites tops (projected surface area) which is lower than the geometrical surface area of the electrode (see Fig. 3b). The fact that the limiting currents of $\text{Fe}^{(II)}$ reduction in chloride medium, using VC electrodes, are lower than those using gold can be simply explained by a reduced electroactive surface area associated with iron dendritic growth on the VC electrodes, but not on the gold electrode.

In Mohr's salt medium, similar magnitudes of the pseudo-limiting current were measured for gold and VC electrodes (cathodic backward scans in Fig. 1a, corresponding to the reduction of $\text{Fe}^{(II)}$ on the substrate covered by the iron electrodeposit). This different behaviour is explained by the very slight difference in iron electrodeposit morphologies (comparatively to chloride medium) obtained on gold and on VC electrodes (Fig. 1, pictures 1–3).

3.1.4. $\text{Fe}^{(II)}/\text{Fe}^{(0)}$ kinetics on the gold electrode

In addition to the differences observed in the limiting current for the three electrode materials, differences also appear between gold and VC electrodes for low currents, on the backward cathodic curves ($\text{Fe}^{(II)}$ reduction) on electrodeposited iron; while these curves do not overlap in chloride medium (Fig. 1b), they overlap in sulfate medium (Fig. 1a). Moreover, in chloride medium (Fig. 1b), the backward curves for VC1 and VC2 overlap and exhibit lower overpotential (activation area starting at ~ -0.9 to ~ -1.05 V/SCE) in comparison to the backward curve obtained using the gold electrode (higher overpotential, activation area starting at ~ -0.95 to ~ -1.15 V/SCE). The iron electrodeposits morphology (Fig. 1, SEM pictures 4–6) could explain the surprising lower overvoltage observed on VC electrodes; indeed, the iron electrodeposit on the gold electrode (picture 6 in Fig. 1) is more uniform but not really 'massive', while iron electrodeposited on VC electrodes (pictures 4 and 5 in Fig. 1) presents micrometric dendrites in a metallic iron 'massive' or bulk form.

The effect of the potential scan rate on the current-potential curves shape, as well as on the deposit structure, for the reduction of $\text{Fe}^{(II)}$ on gold substrate, was examined in Fig. 4. Decreasing potential scan rates (20 \rightarrow 8 \rightarrow 2 mV/s) led to an increase in the amount of iron produced during the cathodic scan (5.7 \rightarrow 14.7 \rightarrow 62.7 mC). Consequently, SEM pictures in Fig. 4b and 4c of iron deposit, produced on the gold substrate during a cathodic scan, show that increasing the amount of iron deposit leads to a change in its structure.

As previously mentioned, iron deposits produced on gold during the cathodic scan, spread on the electrode surface as a thin layer. The SEM picture (Fig. 4c) reveals that for a scan rate of 20 mV/s , the thickness of the deposit is about 90 nm which is close to the

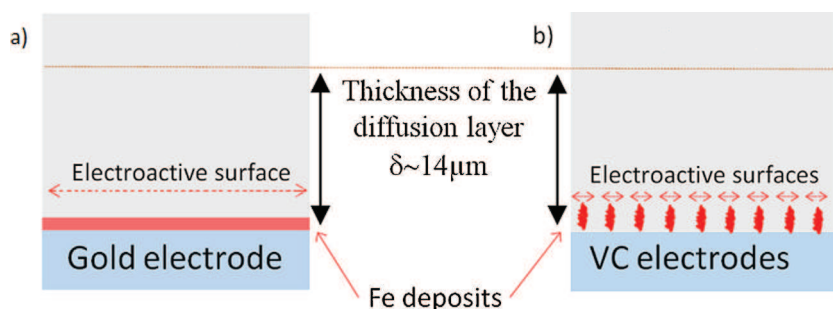


Fig. 3. Schematic representation of the iron electrodeposit morphologies obtained in chloride medium. a): on the gold electrode (related to the SEM pictures 6 in Fig. 1), b): on the VC1 and VC2 electrodes (related to the SEM pictures 4–5 in Fig. 1).

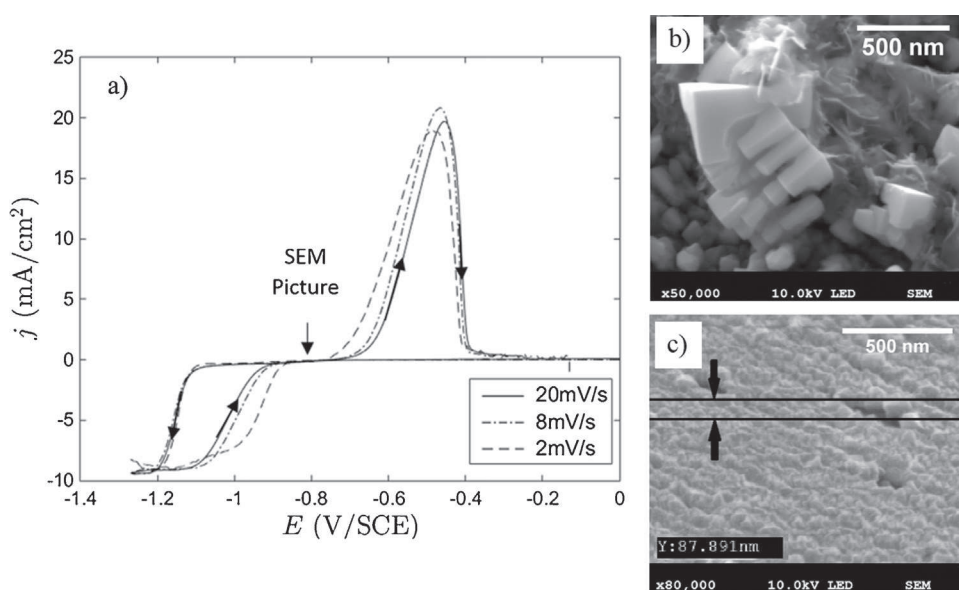


Fig. 4. a) Potential scan rate dependence of the voltamperometry curves (forward and backward, see arrows in a)) obtained on a rotating gold disk electrode, immersed in the FeCl_2 solution. SEM pictures of iron electrodeposit obtained on gold after a cathodic cycle (starting at 0.2 V/SCE, reversed at -1.25 V/SCE, stopped at -0.8 V/SCE) at b) 8 mV/s and c) 20 mV/s.

calculated thickness: equivalent compact layer thickness $e = (M_{\text{Fe}} \int I \cdot dt) / (2F\rho_{\text{Fe}}S_{\text{disk}}) = 67 \text{ nm}$. This confirms the spreading of iron and a 2D growth of the deposit on the gold electrode. A 3D growth of the deposit is obtained only when a larger quantity of iron is deposited (Fig. 4b) for low scan rates 8 mV/s and 2 mV/s. As a first step, iron spreads on the gold surface and once the surface is totally covered, deposit starts to grow following a 3D growth mode and dendritic morphology appears. Indeed, decreasing the scan rate from 20 mV/s to 8 mV/s leads to a change from a homogeneous and ultrathin deposit (Fig. 4c) to a micrometric and dendritic deposit that can act as a bulk iron electrode (Fig. 4b).

The $I=f(E)$ curves obtained for the three scan rates (Fig. 4a) are similar to those indicated in Fig. 1b; the forward cathodic scans exhibit a diffusion-limited plateau at -1.2 V/SCE for which the magnitude of the limiting current is not affected by the potential scan rate. This means that for the three curves the system operates in a steady state; the limitation of the current is due to the constant agitation applied. Concerning the backward cathodic scan, the curves show that, decreasing the potential scan rate (20 → 8 → 2 mV/s) causes the half-wave potential of the $\text{Fe}^{(II)}$ reduction on native iron, to shift to the anodic values (-1.014 → -0.992 → -0.938 V/SCE). This fact suggests a system which tends to become more reversible (to reach the behaviour of a 'bulk iron' electrode) at low scan rates, because for longer electrolysis durations the

amount of iron deposited is higher and a dendritic structure (of micrometric size) is obtained.

Therefore the shape of the cathodic curves is dictated by the structure of iron deposited and therefore by the quantity of iron produced.

Potential scan rate also affects the potential of the oxidation of the iron-deposit signal; the more the scan rate decreases (20 → 8 → 2 mV/s), the more the oxidation of the iron deposited on the gold electrode becomes easier (-0.550, -0.566 and -0.598 V/SCE), suggesting a 'bulk iron behaviour'.

It can be concluded that the electrodeposit obtained at 20 mV/s is so thin (67 nm) that its electrocatalytic properties are affected by the electronic collector (gold) and the $\text{Fe}^{(II)}$ reduction (and oxidation) appears as a slower system. This effect is not observed on VC electrodes because, even at 20 mV/s, the corresponding iron electrodeposits consists of micrometric iron dendrites, which are in a bulk iron form (Fig. 1, SEM pictures 4 and 5).

3.2. Iron electrodeposition by cyclic scan voltammetry under ultrasonification

The electrochemical behaviour of $\text{Fe}^{(II)}$ during ultrasonification was investigated in chloride and sulfate media and for the three electrodes polished with the finest alumina suspension (0.3 μm): VC1, VC2 and gold. The electrochemical cell was immersed in the

ultrasonic bath and special care was taken to always put the cell in the same place in the bath so as to generate the same ultrasound intensity into the cell. Cyclic voltammetry was performed under ultrasonication or under silent conditions and the solution was continuously stirred ($\omega = 1000$ rpm, potential scan rate = 20 mV/s). Results are given in Fig. 5. As previously, forward scan starts from the open circuit potential (OCP $\sim +0.2$ V/SCE) and goes to the cathodic direction (to -1250 mV/SCE for the gold electrode and to -1350 mV/SCE for VC electrodes); then the scan was reversed to potentials of around 0 V/SCE in order to get the backward 'cathodic and anodic parts' of the $I=f(E)$ curve.

3.2.1. Effect of ultrasound on mass transport during iron electrodeposit growth

Current-potential curves obtained under ultrasonication (Fig. 5) exhibit higher $\text{Fe}^{(II)}$ reduction limiting currents (obtained during backward scan) than those obtained under silent conditions (with the exception of current-potential curves in Fig. 5c which will be discussed below). This is due to ultrasounds that induce cavitation bubbles and acoustic streaming, causing additional convection near the electrode and then increasing the mass-transport flux of the electroactive species [20–25,19]. Current fluctuations, that are highly visible, especially on the diffusion-limited plateau of $\text{Fe}^{(II)}$ reduction (see Fig. 5a, b, e and f), are attributed to successive events of the collapse of cavitation bubbles

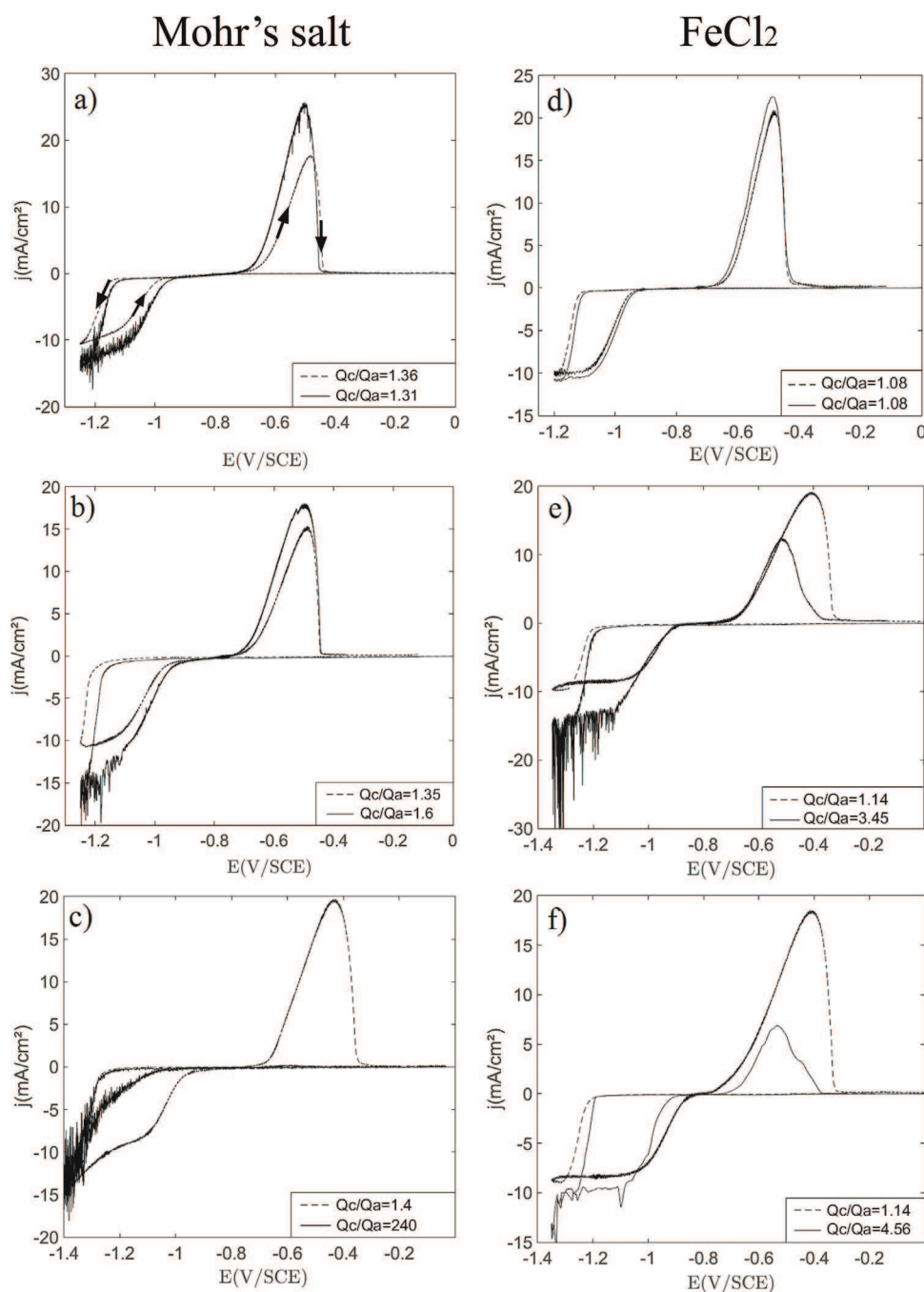


Fig. 5. Cyclic voltammetry scans (forward and backward, see arrows in a)) obtained on a rotating disk electrode for three different materials: gold (a) and d)), VC1 (b) and e)) and VC2 (c) and f)). Curves in a), b) and c) obtained with Mohr's salt solution; curves in d), e) and f) obtained with FeCl_2 solution. Dashed lines: silent conditions, solid lines: ultrasound activated. The ratio between the cathodic charge Q_c , and the anodic charge Q_a , is given for each case in the legend.

close to the electrode surface inducing local and transient vigorous stirring ([21,26,27]). It is interesting to note that for current lower than the limiting current, in the activation area (during backward scans, reduction of $\text{Fe}^{(II)}$ on $\text{Fe}^{(0)}$), current fluctuations are not observed (Fig. 5a, b, c, e and f) and the curves, with and without ultrasound, tend to overlap (especially in Fig. 5b and e). This is in agreement with previous studies showing that ultrasounds affect electrochemical processes mainly via mass-transport enhancement and only slightly the electrode kinetics [39,20,30].

The increase in limiting current of $\text{Fe}^{(II)}$ reduction on the gold electrode in chloride medium, when ultrasounds are activated (Fig. 5d), is low (relative increase of 7%), compared to the other ones corresponding to curves in Fig. 5a, b, e and f (relative increase from 15 to 60%). On the basis of electrodeposited iron morphology obtained by SEM imaging (Fig. 1, pictures 1–6), it appears that the electrodeposit that has grown on the gold electrode in chloride medium and under silent conditions (Fig. 1, pictures 6) is the only one to grow as a thin film. For all other $\text{Fe}^{(II)}$ salts and electrode material combinations, electrodeposited iron presents micrometric dendrites reaching about $1\ \mu\text{m}$ height (Fig. 1, pictures 1–5). Submitting the solution to ultrasounds causes an increase in the limiting current associated with the decrease in diffusion layer thickness [21,22]. Furthermore, the fast growth of the iron electrodeposits probably leads to higher dendrites with heights greater than $1\ \mu\text{m}$, similar to the thickness of the diffusion layer. Consequently, the electroactive surface area increases leading to a current magnitude increase (see the schematic representation in Fig. 6). For electrodeposit growth as a film (the dendritic growth is delayed and such a coupling is not expected), the electroactive surface area remains equal to the geometrical surface area of the electrode and the current increases only due to the enhancement of mass transport by ultrasounds. Therefore, this analysis allows to give an explanation for the observed differences in the limiting current increases with ultrasounds between the thin film growth mode and the dendritic growth mode.

3.2.2. Effect of ultrasound on iron electrodeposits dispersion

The integration of both cathodic (forward and backward) waves and anodic peak (Fig. 5) allow to get the amount of charge for $\text{Fe}^{(II)}$ reduction, Q_c , and for $\text{Fe}^{(0)}$ oxidation Q_a . The computed values of the ratio Q_c/Q_a are given in legends of Fig. 5. Q_c/Q_a values, higher than 1 in all cases, are used below as criterion to discuss the effects of adhesion and ultrasound on iron electrodeposits dispersion from the electrode.

In absence of ultrasonification, Q_c/Q_a obtained in FeCl_2 (~ 1.10) is lower than those obtained in Mohr's salt (~ 1.35), because of the co-reduction of both H^+ and partially of water during the $\text{Fe}^{(II)}$ reduction (as already said in section 3.1.1). Note that the current consumption by H^+ and water reduction constitutes a drawback (loss in faradic yield for $\text{Fe}^{(II)}$ reduction), but also two advantages: i) consumption of H^+ in the diffusion layer, so limitation of the corrosion of zero-valent iron deposit, and ii) production of a little part of H_2 which allows limitation of the oxidation by the residual oxygen.

Concerning the adhesion/dispersion of the iron electrodeposit on the gold electrode (Fig. 5a and d), the effect of the ultrasounds appears minor in both FeCl_2 and Mohr's salt media; indeed comparison of the ratio Q_c/Q_a (see legends in Fig. 5a and d) with ultrasonification (1.31 in Mohr's salt; 1.08 in FeCl_2) and without (1.36 in Mohr's salt; 1.08 in FeCl_2) shows very similar values, demonstrating that all iron electrodeposited during $\text{Fe}^{(II)}$ reduction remains on the gold surface and oxidizes totally during the backward anodic scan. Conversely, for VC electrodes (see Fig. 5b, c, e and f), iron electrodeposits dispersion is observed in every case, Q_c/Q_a obtained with ultrasound is at least equal to 1.6 and it is always higher than Q_c/Q_a values obtained under silent conditions (Fig. 5b, c, e and f).

Note that for the electrolyses using the Mohr's salt solution and the VC1 electrode (Fig. 5b), even if the removal of the deposit is observed ($Q_c/Q_a = 1.6$), the anodic peak (and also the amount of charge), when ultrasounds are activated, is higher than the one obtained under silent conditions. As discussed in [30] and [31], this is due to the enhancement of mass-transfer by ultrasound leading to larger deposition rate and then a larger quantity of iron is formed on the electrode compared to the silent condition case even if some part of the deposit is dispersed.

Iron electrodeposit appears to adhere much more on the gold electrode surface than on the VC electrodes surfaces, because of the high adhesion energy between both metals; the solid deposit requires higher ultrasonification power to be removed and dispersed in the liquid. These results are in agreement with estimation of works of adhesion presented in the Appendix: work of adhesion of iron on gold $W_{\text{Fe}/\text{Au}} = 148.7\ \text{mJ}/\text{m}^2$ and work of adhesion of iron on VC $W_{\text{Fe}/\text{VC}} = 17.3\ \text{mJ}/\text{m}^2$.

Concerning VC1 electrode (Fig. 5b and e), similar curves and Q_c/Q_a ratio are obtained in Mohr's salt and in FeCl_2 . For Mohr's salt, Q_c/Q_a reaches 1.6 with ultrasound, and the main part of the iron deposit (62.5%) remains on the VC1 electrode surface even under ultrasonification. For FeCl_2 , ultrasonification appears to be

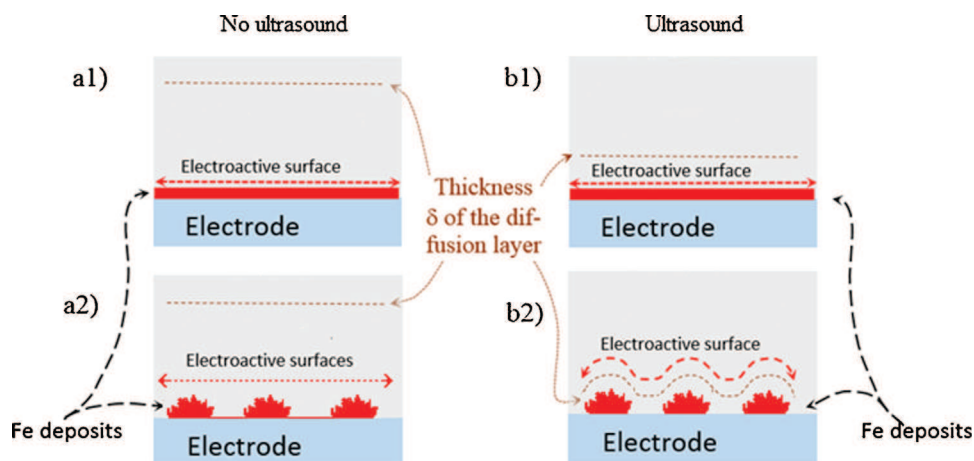


Fig. 6. Schematic representations of possible diffusion layer configurations for the two main types of iron electrodeposit morphology encountered, thin film (a1 and b1) and dendritic (a2 and b2), under silent conditions (a1 and a2) and with ultrasonification (b1 and b2).

more efficient, Q_c/Q_a reaches 3.45 with ultrasounds. Nevertheless, ultrasonication effect on iron deposit dispersion appears less efficient on VC1 than on VC2 (see Fig 5b, c, e and f). Indeed, VC2 electrode led to the most interesting results (Fig. 5c and f) particularly with Mohr's salt solutions (Fig. 5c). The anodic peak corresponding to the remaining iron, electrodeposited during the cathodic scan, is missing, indicating that all the iron electrodeposit was removed from the electrode surface and Q_c/Q_a reaches 240 (instead 1.4 without ultrasound)! In addition, the backward cathodic scan (Fig. 5c) tends to overlap the forward cathodic scan, meaning that $\text{Fe}^{(II)}$ reduction takes place on an almost clean/bare surface, where iron electrodeposits are rapidly and continuously removed thanks to ultrasounds. Iron electrodeposits adhesion on VC2 electrode surface is very weak and they are dispersed easily during their formation. The same effect, even less important (in comparison with the Mohr's salt), is observed with FeCl_2 on VC2 (Fig. 5f), Q_c/Q_a reaches 4.56 under ultrasonication.

A similar analysis of the evolution of the ratio Q_c/Q_a as a function of the ultrasound intensity has been achieved in [30] for the electrodeposition of metals (Zn, Co, Pb and Hg) on a VC electrode using a face-on configuration. The overlapping of both the cathodic backward and the forward scans (as observed in the present study, Fig. 5c) was not observed in this last study, even for the higher ultrasound intensity. This suggests that electrodeposited metals particles were always present on VC electrode surface during the cathodic part of the scan. As discussed in [30] (see also [31]), the dispersion rate was not sufficiently high to overcome the deposition rate during the cathodic part of the scan. The experimental configuration, used in the present study, clearly shows that iron particles can be very rapidly removed by ultrasound allowing to operate continuously (with an almost 'bare' substrate).

This last observation is important from a practical point of view because it shows that it is possible to drive the electrodeposition of iron simultaneously with its almost total dispersion that should lead to the continuous synthesis of fine iron particles (limiting their growth). On another side, as it could be seen in Fig. 5c, the cathodic charge is lower than in the other cases, leading to a lower synthesis rate. As discussed, in [30] and [31], the competitive effect of metal deposition and its dispersion could be adjusted by the

control of both the $\text{Fe}^{(II)}$ concentration and the ultrasound intensity.

To sum up, main differences in the dispersion of iron electrodeposited on gold and VC electrodes, are due to a difference in work of adhesion between iron and these substrates.

However, differences can also be observed between apparently similar VC electrodes: VC1 and VC2. Dispersion by ultrasonication is more efficient on VC2 than on VC1, suggesting that iron adheres less on VC2 than on VC1. To demonstrate this assumption, contact angle measurement were achieved for VC1 and VC2, and results were indicated in Table 1, giving γ_{VC1} and γ_{VC2} .

The values of the surface tensions of VC1 and VC2 electrodes are very similar ($\gamma_{VC1} \sim \gamma_{VC2}$, averaged value = 30 mJ/m^2). γ_{VC2} is found to be slightly higher than γ_{VC1} probably because of a slight difference in their chemical compositions (see section 2.1) and this could induce a better adhesion on VC2 than on VC1 (see Appendix). Nevertheless, experiments have clearly shown a better adhesion on VC1 than on VC2, implying another parameter as responsible of this observed difference. The effect of the VC electrodes surface roughness is analyzed in the following sections.

3.3. Influence of the roughness of the VC electrode on the dispersion of electrodeposited iron

The roughness of the surface of the electrode is a parameter which could influence the adhesion of iron. Both VC electrodes' surface were characterized by optical microscopy and by an interferometric surface profiler (Zygo 3D), Fig. 7. The small void inclusions within the VC1 (visible as holes on its surface with diameters in the range 1 to $10 \mu\text{m}$, Fig. 7b and 7-2) correspond to manufacturing defects. Conversely, VC2 does not exhibit holes on its surface; remaining polishing stripes are visible on the surface profile and their heights remain less than 30 nm (Fig. 7-1).

Decreasing the roughness of the electrode surface enables easier electrodeposit dispersion in the liquid. In order to specifically study the effect of the electrode roughness on electrodeposit dispersion, independently of iron growth, in the next section we focus on the dispersion kinetics of iron electrodeposited under silent conditions.

Iron deposition was achieved by galvanostatic electrolysis under silent conditions using the rotating disk electrode ($\omega = 1000$

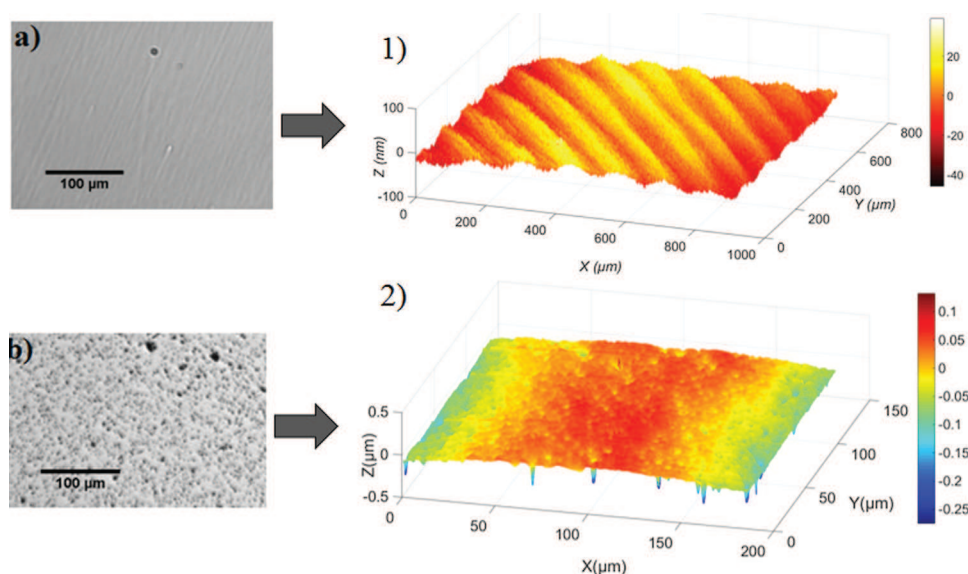


Fig. 7. Optical images and surface profiles of the polished (alumina suspension at $0.3 \mu\text{m}$) VC electrodes used in the present study; for VC2 a) optical image and 1) surface profile; for VC1 b) optical image, 2) surface profile.

rpm) and the same electrolytes composition. In order to avoid significant hydrogen production, the applied current, $I_{applied}$, corresponds to 90% of the limiting current, I_{lim} , obtained during the backward cathodic scan under silent conditions. The duration of electrolysis Δt was chosen in order to obtain an iron electrodeposit with an equivalent iron-compact-layer of 85 nm. After electrolysis, the rotation of the depolarized disk electrode (cathode disconnected from the anode), was maintained and ultrasonication was immediately activated (or not) for a specific duration t_{US} . In order to evaluate the effect of ultrasonication on the dispersion of the deposit, an anodic scan was immediately carried out after the ultrasonication phase (from the OCP ~ -0.730 V/SCE to $+0.2$ V/SCE at 20 mV/s, maintaining electrode rotation and without ultrasonication).

The amount of charge (Q_a) corresponding to the oxidation of the remaining deposit on the electrode surface was then evaluated. Note that Q_a was compared with an amount of charge, thus called $Q_{a,ref}$, which was measured during a 'reference anodic scan without ultrasounds'; $Q_{a,ref}$ corresponds to the oxidation of the iron deposit not submitted to ultrasonication ($t_{US}=0$) after electrolysis. The results obtained for the operating parameters investigated are presented in Fig. 8, where the ratio ($Q_a/Q_{a,ref}$) is plotted as a function of t_{US} . Points on each curve correspond to the average values $Q_a/Q_{a,ref}$ measured for at least three experiments; error bars correspond to standard deviations. As indicated above, the iron deposit on the gold electrode is not affected (or very slightly) by ultrasounds; there is no dispersion. For this reason, this section focuses on the vitreous carbon electrodes VC1 and VC2 only, and it presents the effect of both precursors ($FeCl_2$ and Mohr's salt) on the dispersion of the solid iron deposit. The curves $Q_a/Q_{a,ref}$ versus t_{US} (Fig. 8) are analyzed with the help of SEM pictures of the

electrodeposited iron not submitted to ultrasonication (insets in Fig. 8).

3.3.1. Iron electrodeposits morphology

The Morphology of iron electrodeposits formed by galvanostatic electrolysis (insets in Fig. 8) is different from those formed by voltammetry (Fig. 1). For $FeCl_2$ and both VC1 and VC2 (insets in Fig. 8a and b), electrodeposited iron morphologies consist of micrometric 'rounded particles' and submicrometric iron structures covering the remaining VC surfaces, while dendritic structures were obtained with voltammetry. It can be noticed that the rounded particles have coalesced in some cases, forming bigger flakes. This is clearly observed on the VC2 electrode (inset in Fig. 8b).

The morphologies obtained by galvanostatic electrolysis appear more 'homogeneous' (less dendritic) than the ones obtained by voltammetry. Among other effects, this could be attributed to the electrodeposition mode and the cathodic current employed; with voltammetry, electrodeposition is conducted under continuous evolution of the applied voltage and the resulting current (which reached its limiting value), while galvanostatic electrolyses carried out with a current close (90%) to the limiting current. As often observed in galvanostatic electrodeposition, electrodeposit tends to be dendritic/powdery when applied current is equal to, or higher than the limiting current ([40–42]). Even when the applied current is just below the limiting current, a 'less rough' and 'less dendritic' electrodeposit morphology could be obtained [41,42].

For Mohr's salt and both VC1 and VC2 (insets in Fig. 8c and d), metallic iron takes the form of micrometric structures as for the deposition obtained by voltammetry; but here, these micrometric structures seem to have grown under the form of a ramified

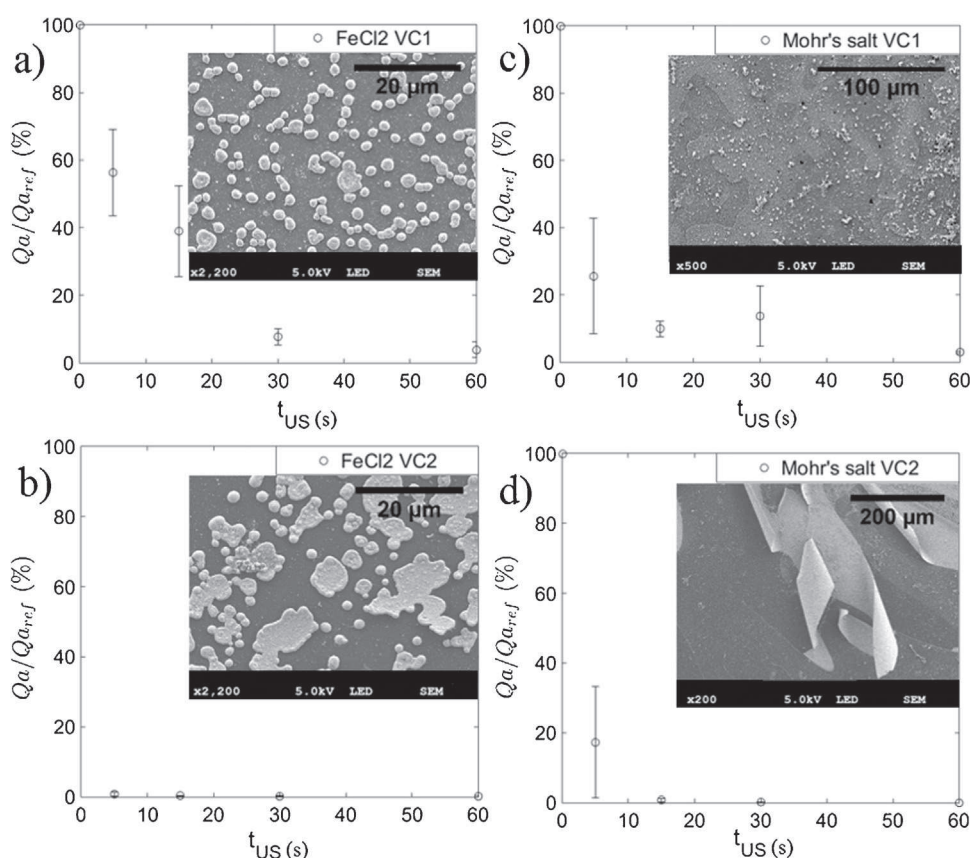


Fig. 8. Dimensionless iron quantity $Q_a/Q_{a,ref}$ remaining on the electrode as a function of the ultrasonication duration (t_{US}). Experiments a) (VC1) and b) (VC2) were achieved in the $FeCl_2$ solution. Experiments c) (VC1) and d) (VC2) were achieved in the Mohr's salt solution. Points correspond to the average values $Q_a/Q_{a,ref}$ measured for at least three experiments; error bars correspond to standard deviations. Insets: SEM images of the electrodeposits just after the electrolysis (not exposed to ultrasonication).

structure covering all the substrate surface. For the VC2 electrode (inset in Fig. 8d), a proportion of the iron deposit partially peeled off the electrode surface, probably solely due to the effect of electrode rotation. Comparatively, the iron deposit from Mohr's salt on VC1 (inset in Fig. 8c) consists of the same deposit morphology but it remains stuck on the electrode surface.

In the FeCl_2 media, it seems that these iron particles (especially the flattened ones, inset in Fig. 8b) also partially peeled off the electrode surface in the case of VC2 electrode. Therefore, these SEM images, taken just before the ultrasound phase, show that the adhesion of iron electrodeposits to the electrode seems to be weaker for the VC2 than for VC1. Indeed, in the following section, this observation is confirmed by electrochemical measurements indicated on the plot of Qa/Qa_{ref} as a function of t_{US}

3.3.2. Dispersion by ultrasonification of iron 'electrodeposited under silent conditions'

3.3.2.1. Ultrasound action for two VC substrates and two salt precursors.

The effect of the substrate (VC1 and VC2) on the iron dispersion for both FeCl_2 and Mohr's salt precursors were examined. All the curves (except Fig. 8b) exhibit a decrease of the ratio Qa/Qa_{ref} as a function of t_{US} , meaning that the quantity of the dispersed iron increases progressively with time during ultrasonification.

For all experiments, an ultrasonification duration of 60 s allows the removal of most ($\sim 90\%$) of the iron deposit, and disperses it into the liquid. Standard deviation of the ratio Qa/Qa_{ref} has been determined in both media and with both substrates. For short ultrasonification time, results are not highly reproducible, but they become more reproducible for longer durations. Furthermore, the quantity of the iron deposit remaining on the substrate decreases progressively with time; this is particularly visible for the VC1 electrode (Fig. 8a and c). For the VC2 electrode, dispersion is too fast to observe this behavior, especially in the case of FeCl_2 medium (Fig. 8b).

The progressive removal of iron from the VC1 electrode is explained by the operated mode of ultrasonic dispersion. Indeed, constant-power-ultrasound produces cavitation bubbles in the liquid at a constant rate per unit of volume. However, only the collapses of cavitation bubbles in the vicinity of the iron deposit surface can cause its local dispersion. The flux of removed particles should then be proportional to the quantity of iron deposit present on the electrode surface. Thus, decreasing the iron quantity at the surface, reduces the removed particles flux, as observed experimentally. A simple first order kinetics model can be built to

quantify this behavior:

$$\frac{d}{dt} \left[\frac{Qa}{Qa_{ref}} \right] = -s \frac{Qa}{Qa_{ref}}, \quad (5)$$

with s being the dispersion rate constant (s^{-1}) that should depend on the ultrasound power, on the adhesion energy $E_{adh} = W_{Fe/VC} S_{Fe/VC}$ ($S_{Fe/VC}$ being the surface area of the iron/VC interface) and on the size and distribution of particles on the electrode. Equation (5) leads to the exponential decrease: $Qa/Qa_{ref}(t) = \exp(-st)$. The plot of $\ln(Qa/Qa_{ref})$ versus t_{US} using data from Fig. 8a and c are shown in Fig. 9. Dispersion around the linear best fit curves is observed (due to the results that are not totally reproducible). Nevertheless, it should be pointed out that this very simple model captures the overall dynamic of the phenomenon.

This result is in agreement with results from other studies, mentioning a progressive 'erosion/roughing' of Pt electrode submitted to ultrasonification [28], or a progressive ablation associated with cracks formation in glass surrounding a disk electrode submitted to ultrasound [32].

In both media, results indicate that the iron deposit was more easily removed from the VC2 than from the VC1 electrode, after 15 s of ultrasonification, 100% of the iron deposit is dispersed, confirming what has been observed previously on the basis of SEM images in insets of Fig. 8. In comparison, on VC1, $\sim 60\%$ (in FeCl_2) and $\sim 90\%$ (in Mohr's salt) is removed after 15 s of ultrasonification (Fig. 8).

The above observed differences in iron adhesion on VC1 and VC2 cannot be explained by differences in the work of adhesion between iron and VC substrates ($W_{Fe/VC}$ in J/m^2). As also indicated above, another difference between VC1 and VC2 electrodes is their surface roughness'. Micrometric holes on VC1, that induce a higher roughness (Fig. 7), act as 'anchors' for the electrodeposited iron. Roughness induces higher iron/VC interface surface area $S_{Fe/VC}$ leading to higher adhesion energy, $E_{adh} = W_{Fe/VC} S_{Fe/VC}$, as said before. 'More cavitation bubbles' (which provide mechanical energy) are then required to detach the iron particles from the electrode, which takes more time (using always the same ultrasound power) and leads to a slower iron removal as experimentally observed.

3.3.2.2. Effect of different polishing level on deposit dispersion.

In order to confirm the effect of the electrode roughness on iron deposit adhesion, three different polishings were applied to the VC2 electrode surface: the substrate was polished with paper grid P800 (electrode VC2P800), P1200 (electrode VC2P1200) and with $0.3 \mu\text{m}$ alumina suspension (electrode VC20.3 μm). As previously

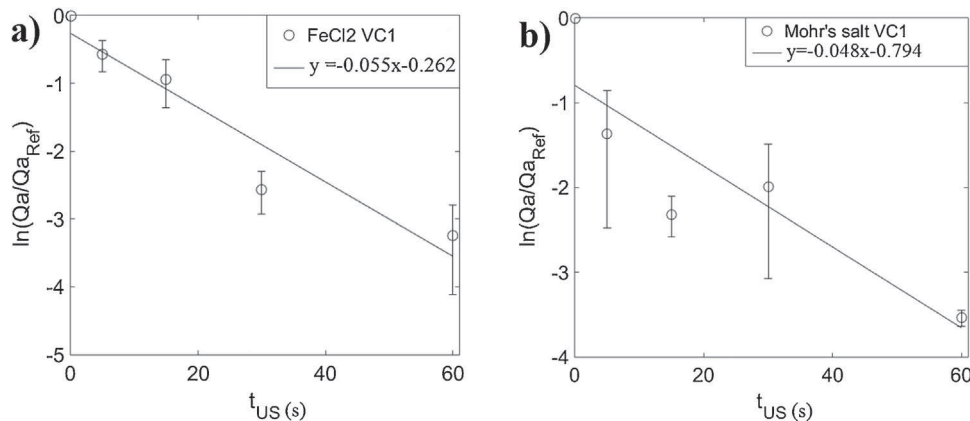


Fig. 9. $\ln(Qa/Qa_{ref})$ versus ultrasonic time t_{US} on VC1 (circles) for a) FeCl_2 and b) Mohr's salt, from data of Fig. 8a and c. Solid lines correspond to best linear fits.

stated, the electrodes surfaces were characterized using an optical surface profiler (Zygo 3D) and results are shown in Fig. 10. Due to mechanical polishing stripes are clearly visible for all levels of polishing. The one dimensional profiles, presented in Fig. 10, show a peak-to-peak amplitude of approximately 2 μm and 1 μm for VC2P800 and VC2P1200 respectively. On VC2, polished with the 0.3 μm alumina suspension, the surface appears to be smoother, presenting a peak-to-peak amplitude of approximately 0.03 μm . The values of the Wenzel's roughness r_w and the arithmetic roughness r_a are given in Table 2.

Iron electrodeposits obtained after galvanostatic electrolysis on VC2, polished with P800 and P1200 paper, are presented in Fig. 11a (insets). The effect of the ultrasonification duration on iron dispersion was examined by plotting of the ratio ($Q_a/Q_{a,ref}$) as a function of t_{US} (Fig. 11a), for the three different polishing levels. As for VC1 (Fig. 8a and c, and Fig. 9), a practically exponential decrease was observed, that validates the fact that iron electrodeposit dispersion by ultrasonification follows a first order kinetics (Equation 5). The lowest dispersion efficiencies are indeed obtained for electrodes that present the highest roughness. For example, after 5 s of ultrasonic duration, the quantity of iron deposit remaining on the surface for VC2, decreases from $\sim 45\%$ to $< 5\%$ when polishing was achieved respectively with paper grid P800, P1200 and 0.3 μm alumina suspension. This confirms the effect of the roughness on the dispersion kinetics.

For VC2P800 and VC2P1200, the same quantity of iron was deposited during the electrolyses, but as r_w (ratio between actual surface and geometrical surface) is higher for VC2P800 than for VC2P1200 (Table 2), $S_{Fe/VC}$ is larger for VC2P800 than for VC2P1200. This induces a larger $E_{adh} = W_{Fe/VC} S_{Fe/VC}$ for

Table 2

VC2 surface roughness' for different levels of polishing: with 0.3 μm alumina suspension, with paper grid P800 and P1200.

	Amplitude max (μm)	r_w	r_a (nm)
VC20.3 μm	0.03	1.0000	8
VC2P1200	1	1.0156	162
VC2P800	2	1.0371	345

VC2P800 and then a slower dispersion kinetics, as observed in Fig. 11a.

Deposits obtained on these rough surfaces can be compared with deposits obtained on a smooth VC2 electrode (polished with 0.3 μm alumina suspension, inset of Fig. 8b). On the smooth surface, iron is deposited randomly, forming rounded particles and micrometric plates/flakes (Fig. 8). On the rough surfaces (VC2P800 and VC2P1200), micrometric plates are also observed, but they grow along the stripes, following the topography of the substrates. Furthermore, SEM pictures, taken with 40° tilt, show that iron preferentially grows at the bottom of the stripes (Fig. 11b).

This behaviour does not correlate with the classical phenomenology of galvanostatic electrodeposition on rough substrates. When the diffusion layer thickness ($\sim 14 \mu\text{m}$ here) is greater than the height of the stripes (2 μm here, *macroprofile*), due to local variations of the diffusion layer thickness, metal should be preferentially deposited at the top of the stripes [41]. We cannot explain this observation at this time. However, linear voltammetry conducted on these three surfaces reveals that the greater the roughness, the lesser the overpotential of initial $\text{Fe}^{(II)}$ reduction (not shown). By analogy with the analysis undertaken in section 3.1.2, this fact suggests that polishing stripes offer an area

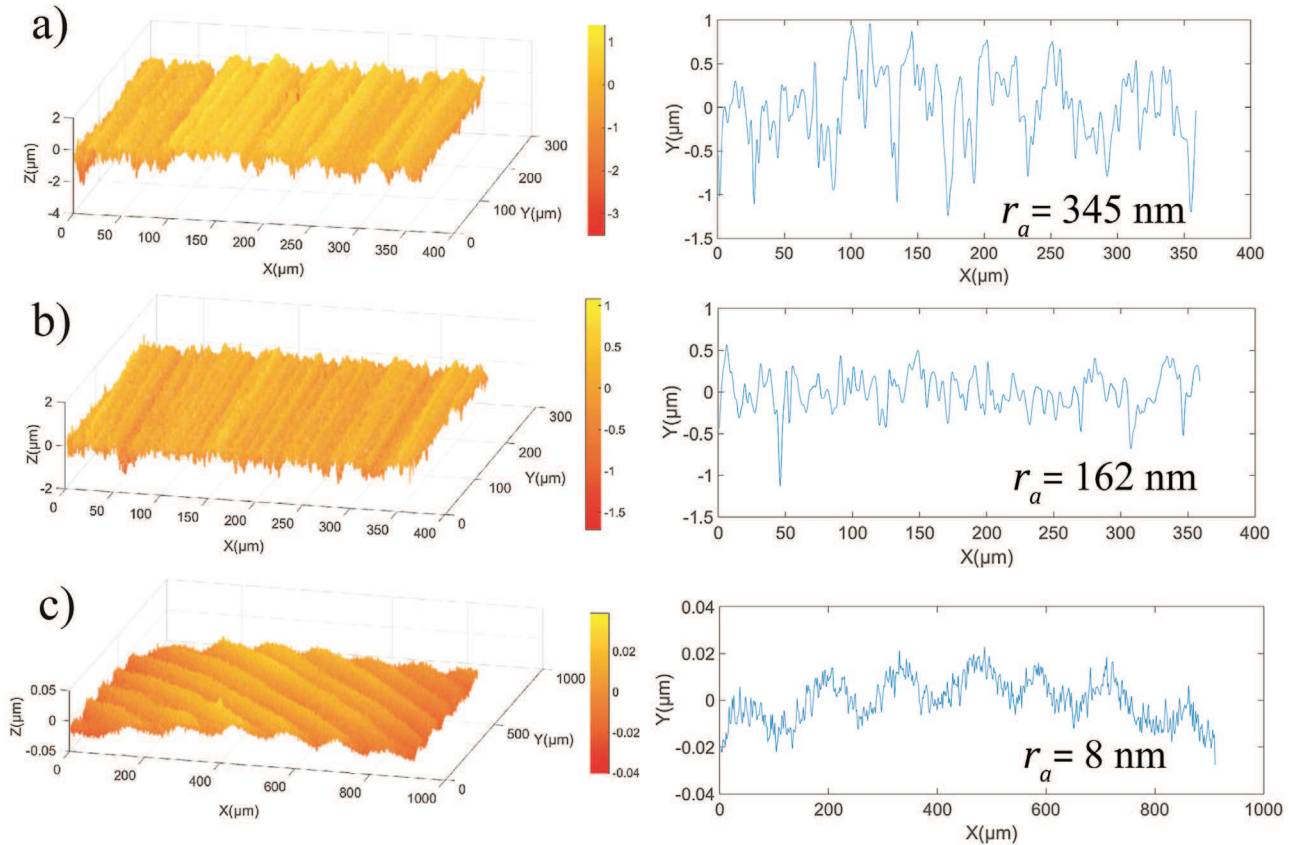


Fig. 10. Surface profiles of VC2 electrodes obtained by an optical surface profiler (Zygo 3D) and their one dimensional profiles (perpendicular to the stripes), a) VC2P800, b) VC2P1200, c) VC20.3 μm .

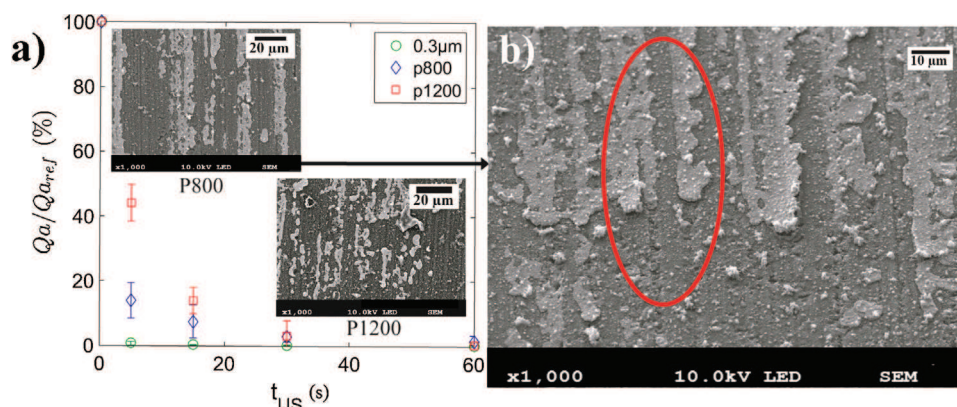


Fig. 11. Dimensionless iron quantity (Qa/Qa_{ref}) remaining on the electrode as a function of the ultrasonication duration (t_{US}) for VC2 in $FeCl_2$ solution for various polishing levels. Points correspond to the average values Qa/Qa_{ref} measured for at least three experiments; error bars correspond to standard deviations; **insets** show SEM images of the electrodeposits just after the electrolysis (not exposed to ultrasonication) on VC2 polished with P800 and P1200 paper grids. b) SEM image with 40° tilt, of the iron electrodeposit on VC2P800; iron deposits located at the stripes bottom are visible in the red ellipse.

where $\gamma_{Fe/VC}$ is lowered, facilitating iron deposition. $\gamma_{Fe/VC}$ should therefore be lower at the bottom of the stripes than at the top, leading to an improved adhesion of these ‘anchored’ deposits ($W_{Fe/VC} = \gamma_{Fe/L} + \gamma_{VC/L} - \gamma_{Fe/VC}$, see the [Appendix](#)).

Another point is that iron deposited onto the stripes can be protected from the fluid stream and ultrasonic perturbation that can cause the detachment of the deposit. Indeed, the same quantity of iron is deposited on the rough substrates (VC2P800 and VC2P1200) as that on the smooth one. But iron deposited inside the stripes of the rough substrates has an iron/liquid interface less exposed to cavitation bubbles.

These results clearly confirm the major importance of VC electrode surface roughness on the adhesion of iron deposit and demonstrate that dispersion kinetics effectively slows down as electrode surface roughness increases.

4. Conclusion

The objective of this work was to study phenomena involved in the synthesis of zero-valent iron nanoparticles by sonoelectrochemistry. The role of the electrode substrate on the morphology of the electrodeposited iron and its dispersion by ultrasound was more particularly investigated, considering the following three key parameters: 1) the interfacial energy of the iron/electrode interface $\gamma_{Fe/elect}$, 2) the work of adhesion of the electrodeposited iron on the electrode and 3) the electrode surface roughness.

Choosing gold or VC as electrode materials, exhibiting different interfacial energies $\gamma_{Fe/VC} > \gamma_{Fe/Au}$, allows to observe significant differences in both the morphology of iron electrodeposits and their dispersion by ultrasound. No dispersion was observed using ultrasound when iron was reduced on the gold; the electrodeposited iron adheres strongly and it spreads easily along electrode surface (2D growth mode) before the eventual starting of a dendritic growth (depending on the precursor salt used). On VC electrodes, electrodeposited iron covers partially the electrode surface (3D growth mode); its weak adhesion facilitates its dispersion by ultrasound.

A particular regime was observed, using the smoother VC electrode during cyclic voltammetry scan under ultrasonication: electrodeposit dispersion is complete, allowing continuous regeneration of the bare substrate; fine iron particles should be synthesized during this process. These results allow to highlight the importance of the electrode material choice for the elaboration of sonoelectrochemical devices dedicated to the synthesis of metallic nanoparticles. The low surface energy and the low affinity

of VC substrates against the deposited metal offer the double benefit:

- to favor the low spreading of the metal on the electrode (3D growth), promoting the formation of isolated fine iron particles instead of thin films
- to facilitate the ‘ultrasound-assisted’ dispersion of the electrodeposit.

The iron electrodeposits dispersion by ultrasound appears to be described by a first order kinetics because of the constant removal action of the cavitation bubbles. Moreover, dispersion kinetics slow down when the electrode surface roughness increases, the latter inducing enhanced adhesion of the iron electrodeposits.

Even if the synthesized quantity of dispersed iron particles is low with the device used (micro-electrolyses), some preliminary electrolyses were carried out (without surfactant) by applying ultrasound (VC2 polished at $0.3 \mu m$, Mohr’s salt). The characterization by dynamic light scattering revealed the presence of ~ 200 nm sized particles.

Acknowledgments

This study was supported by the MSR Graduate Research Fellowship and the authors would like to thank the Paul Sabatier University for funding the research. Thanks are also due to Sophie Chambers for checking the manuscript.

Appendix. Estimation of works of adhesion and interfacial tensions

The objective of this Appendix is to estimate the works of adhesion of iron (Fe) on the electrode materials used in this study, $W_{Fe/elect}$, with *elect* corresponding either to Au (gold) or to VC electrodes. Furthermore, the interfacial tensions of the interface between iron and electrode materials, $\gamma_{Fe/elect}$, are also estimated. $W_{Fe/elect}$ and $\gamma_{Fe/elect}$ are estimated using the following theoretical development and the values of electrode surface energies measured by the contact angle measurement method.

The work of adhesion of iron on the electrode can be estimated considering only the van der Waals interactions and following the theory developed in [43]. Considering the van der Waals interaction potential profile for iron interacting with electrode across the liquid phase, work of adhesion corresponds to the extremum value of this profile. It has been shown, for several

material combinations, that this extremum is found for a separation distance between both interacting media (iron and electrode) $d=0.165$ nm [43]. Work of adhesion can then be estimated using the following equation ([43]):

$$W_{Fe/elect} = A_{elect/L/Fe} / (12\pi d^2), \quad (A1)$$

where $A_{elect/L/Fe}$ is the Hamaker constant for iron and electrode interacting across the liquid (L). $A_{elect/L/Fe}$ is computed thanks to the combining relation:

$$A_{elect/L/Fe} = (\sqrt{A_{elect}} - \sqrt{A_L})(\sqrt{A_{Fe}} - \sqrt{A_L}), \quad (A2)$$

where A_{elect} , A_L and A_{Fe} are the computed Hamaker constants from the Lifshitz theory of respectively electrode material, water and iron; the following Hamaker constants values are used: $A_{Au} = 45.3 \times 10^{-20}$ J ([44]), $A_L = 3.7 \times 10^{-20}$ J (Hamaker constant of water, [43]) and $A_{Fe} = 26.0 \times 10^{-20}$ J ([45]). The value of A_{VC} could be estimated using the measured surface energy of the VC electrodes, $\gamma_{VC} = 30$ mJ/m² (averaged value of surface energies measured for VC1 and VC2, see Table 1), and the equation: $A_{VC} = 24\pi d^2 \gamma_{VC}$ ([43]).

Finally, combining equations (A1) and (A2), we find $W_{Fe/Au} = 148.7$ mJ/m² and $W_{Fe/VC} = 17.3$ mJ/m². Even if the obtained value for $W_{Fe/Au}$ is probably underestimated (because attractive forces between metals, such as possible *metallic bonds*, are not considered by the van der Waals interactions), we show that $W_{Fe/Au} \gg W_{Fe/VC}$. Iron should adhere much more on the gold electrode than on the VC electrodes. Indeed, this is effectively demonstrated experimentally, in section 3.2.2.

On the basis of the values of these works of adhesion, interfacial tensions $\gamma_{Fe/elect}$ can be estimated. Indeed, the work of adhesion can be expressed as a function of the interfacial tensions involved in the system using the Dupr e's equation:

$$W_{Fe/elect} = \gamma_{Fe/L} + \gamma_{elect/L} - \gamma_{Fe/elect}, \quad (A3)$$

where $\gamma_{Fe/L}$, $\gamma_{elect/L}$ and $\gamma_{Fe/elect}$ are the interfacial tensions respectively between iron and electrolytic solution (L), between electrode and electrolytic solution and between iron and electrode. $W_{Fe/elect}$ corresponds to the energy per unit area required to separate the iron surface from the electrode surface in the electrolytic solution. Using equation (A3), $\gamma_{Fe/VC} - \gamma_{Fe/Au}$ can be expressed as:

$$\gamma_{Fe/VC} - \gamma_{Fe/Au} = \gamma_{VC/L} - \gamma_{Au/L} + W_{Fe/Au} - W_{Fe/VC} \quad (A4)$$

Girifalco and Good [46] have shown that interfacial tensions can be approximately computed as a function of the surface tensions by:

$$\gamma_{a/b} = \gamma_a + \gamma_b - 2\Phi_{a/b} \sqrt{\gamma_a \gamma_b} \quad (A5)$$

where $\gamma_{a/b}$ is the interfacial tension between phase *a* and phase *b*, γ_a and γ_b are the surface tensions of respectively phase *a* and *b*, $\Phi_{a/b}$ is an adjustment parameter which depends on interactions between *a* and *b*. The relation (A5) is applied for the VC electrode and for the gold electrode interfaces, (respectively $\gamma_{VC/L} = \gamma_{VC} + \gamma_L - 2\Phi_{VC/L} \sqrt{\gamma_{VC} \gamma_L}$ and $\gamma_{Au/L} = \gamma_{Au} + \gamma_L - 2\Phi_{Au/L} \sqrt{\gamma_{Au} \gamma_L}$). γ_L is taken as the pure water surface tension, 73 mJ/m² at 20 °C (i.e. neglecting salts content). As previously, the value 30 mJ/m² is chosen for γ_{VC} . For gold surface, placed in ambient conditions, surface contaminations occur ([47]) and the value of γ_{Au} is then significantly lower than its value measured for pure gold material (~1500 mJ/m² at the melting point, [48]). γ_{Au} has been measured by contact angle measurement, $\gamma_{Au} = 27$ mJ/m² (measured at ± 3 mJ/m²).

The adjustment parameters $\Phi_{Au/L}$ and $\Phi_{VC/L}$ are generally close to 1. Indeed according to the experiments of Girifalco and Good [46], carried out with a lot of material combinations (including mercury as metal), the adjustment parameter lies in the range [0.31, 1.17]. Using extremes values (0.31 and 1.17), interfacial energies $\gamma_{VC/L}$ and $\gamma_{Au/L}$ are estimated as being within the wide range [74.0 mJ/m²; 0 mJ/m²] and [72.5 mJ/m²; 0 mJ/m²] respectively (restricting to positive values).

Finally, applying equation (A4), $\gamma_{Fe/VC} - \gamma_{Fe/Au}$ lies in the range of positive values [205.4 mJ/m²; 58.9 mJ/m²] meaning that $\gamma_{Fe/VC} > \gamma_{Fe/Au}$. Iron should then spreads more on the gold electrode surface than on the VC electrode surface. This is effectively experimentally observed and discussed in section 3.2.1.

However, it should be kept in mind that these estimated values for $\gamma_{Fe/VC} - \gamma_{Fe/Au}$ and $W_{Fe/Au}$ are probably underestimated since, as said above, only van der Waals interactions are considered for the computation of $W_{Fe/Au}$. A 'upper limit' for $W_{Fe/Au}$ can be estimated using the 'apparent' Hamaker constants computed from gold and iron surface tensions ($A_{Fe/Au} = 24\pi d^2 \gamma_{Fe \text{ or } Au}$) taking values corresponding to a 'clean' surface state ($\gamma_{Au} = 1500$ mJ/m² and $\gamma_{Fe} = 2475$ mJ/m², [48]). Then, the value of 3138 mJ/m² is obtained for $W_{Fe/Au}$ suggesting, as expected, strong interactions between iron and the gold electrode.

References

- [1] Y.J. Wang, S.M. Hussain, G.P. Krestin, Superparamagnetic iron oxide contrast agents: Physicochemical characteristics and applications in MR imaging, *Eur. Radiol.* 11 (2001) 2319–2331.
- [2] A. Ito, M. Shinkai, H. Honda, T. Kobayashi, Medical application of functionalized magnetic nanoparticles, *J. Biosci. Bioeng.* 100 (2005) 1–11.
- [3] A. Jordan, R. Scholz, P. Wust, H. F ahling, R. Felix, Magnetic fluid hyperthermia (MFH): Cancer treatment with AC magnetic field induced excitation of biocompatible superparamagnetic nanoparticles, *J. Magn. Magn. Mater.* 201 (1999) 413–419.
- [4] C.G. Hadjipanayis, M.J. Bonder, S. Balakrishnan, X. Wang, H. Mao, G.C. Hadjipanayis, Metallic Iron Nanoparticles for MRI Contrast Enhancement and Local Hyperthermia, *Small* 4 (2008) 1925–1929.
- [5] R.A. Crane, T.B. Scott, Nanoscale zero-valent iron: Future prospects for an emerging water treatment technology, *J. Hazard. Mater.* 211–212 (2012) 112–125.
- [6] C. Wang, W. Zhang, Synthesizing Nanoscale Iron Particles for Rapid and Complete Dechlorination of TCE and PCBs, *Environ. Sci. Technol.* 31 (1997) 2154–2156.
- [7] D.P. Siantar, C.G. Schreier, C. Chou, M. Reinhard, Treatment of 1,2-dibromo-3-chloropropane and nitrate-contaminated water with zero-valent iron or hydrogen/palladium catalysts, *Water Res.* 30 (1996) 2315–2322.
- [8] S. Choe, Y. Chang, K. Hwang, J. Khim, Kinetics of reductive denitrification by nanoscale zero-valent iron, *Chemosphere* 41 (2000) 1307–1311.
- [9] S. Chen, H. Hsu, C. Li, A new method to produce nanoscale iron for nitrate removal, *J. Nanoparticle Res.* 6 (2004) 639–647.
- [10] D.L. Huber, Synthesis, properties, and applications of iron nanoparticles, *Small* 1 (2005) 482–501.
- [11] J.E. Mu oz, J. Cervantes, R. Esparza, G. Rosas, Iron nanoparticles produced by high-energy ball milling, *J. Nanoparticle Res.* 9 (2007) 945–950.
- [12] L.B. Hoch, E.J. Mack, B.W. Hydutsky, J.M. Hershman, J.M. Skluzacek, T.E. Mallouk, Carbothermal synthesis of carbon-supported nanoscale zero-valent iron particles for the remediation of hexavalent chromium, *Environ. Sci. Technol.* 42 (2008) 2600–2605.
- [13] M. Bystrzejewski, Synthesis of carbon-encapsulated iron nanoparticles via solid state reduction of iron oxide nanoparticles, *J. Solid State Chem.* 184 (2011) 1492–1498.
- [14] F. He, D. Zhao, Manipulating the size and dispersibility of zerovalent iron nanoparticles by use of carboxymethyl cellulose stabilizers, *Environ. Sci. Technol.* 41 (2007) 6216–6221.
- [15] J. Delplancke, J. Dille, J. Reisse, G.J. Long, A. Mohan, F. Grandjean, Magnetic nanopowders: Ultrasound-assisted electrochemical preparation and properties, *Chem. Mater.* 12 (2000) 946–955.
- [16] A. Khachatryan, R. Sarkissyan, L. Hassratyan, V. Khachatryan, Influence of ultrasound on nanostructural iron formed by electrochemical reduction, *Ultrason. Sonochem.* 11 (2004) 405–408.
- [17] V. S  ez, T.J. Mason, Sono-electrochemical synthesis of nanoparticles, *Molecules* 14 (2009) 4284–4299.
- [18] J.C. Eklund, F. Marken, D.N. Waller, R.G. Compton, Voltammetry in the presence of ultrasound: a novel sono-electrode geometry, *Electrochim. Acta* 41 (1996) 1541–1547.

- [19] J. Klima, Application of ultrasound in electrochemistry. An overview of mechanisms and design of experimental arrangement, *Ultrasonics* 51 (2011) 202–209.
- [20] D.J. Walton, S.S. Phull, A. Chyla, J.P. Lorimer, T.J. Mason, L.D. Burke, et al., Sonovoltammetry at platinum electrodes: surface phenomena and mass transport processes, *J. Appl. Electrochem.* 25 (1995) 1083–1090.
- [21] J. Klima, C. Bernard, C. Degrand, Sonochemistry: transient cavitation in acetonitrile in the neighbourhood of a polarized electrode, *J. Electroanal. Chem.* 399 (1995) 147–155.
- [22] R.G. Compton, J.C. Eklund, S.D. Page, T.J. Mason, D.J. Walton, Voltammetry in the presence of ultrasound: mass transport effects, *J. Appl. Electrochem.* 26 (1996) 775–784.
- [23] R.G. Compton, J.C. Eklund, F. Marken, T.O. Rebbitt, R.P. Akkermans, D.N. Waller, Dual activation: coupling ultrasound to electrochemistry—an overview, *Electrochim. Acta* 42 (1997) 2919–2927.
- [24] C.E. Banks, R.G. Compton, A.C. Fisher, I.E. Henley, The transport limited currents at insonated electrodes, *Phys. Chem. Chem. Phys.* 6 (2004) 3147–3152.
- [25] B.G. Pollet, J. Hihn, M. Doche, J.P. Lorimer, A. Mandroyan, T.J. Mason, Transport Limited Currents Close to an Ultrasonic Horn, *J. Electrochem. Soc.* 154 (2007) 131–138.
- [26] E. Maisonhaute, P.C. White, R.G. Compton, Surface Acoustic Cavitation Understood via Nanosecond Electrochemistry, *J. Phys. Chem. B* 105 (2001) 12087–12091.
- [27] E. Maisonhaute, B.A. Brookes, R.G. Compton, Surface acoustic cavitation understood via nanosecond electrochemistry. 2. The motion of acoustic bubbles, *J. Phys. Chem. B* 106 (2002) 3166–3172.
- [28] R.G. Compton, J.C. Eklund, S.D. Page, G.H.W. Sanders, J. Booth, Voltammetry in the Presence of Ultrasound. Sonovoltammetry and Surface Effects, *J. Phys. Chem.* 98 (1994) 12410–12414.
- [29] F. Marken, T.O. Rebbitt, J. Booth, R.G. Compton, The Use of Ultrasound in the Enhancement of the Deposition and Detection of Metals in Anodic Stripping Voltammetry, *Electroanalysis* 9 (1996) 19–22.
- [30] M.E. Hyde, R.G. Compton, How ultrasound influences the electrodeposition of metals, *J. Electroanal. Chem.* 531 (2002) 19–24.
- [31] S. Floate, M. Hyde, R.G. Compton, Electrochemical and AFM studies of the electrodeposition of cobalt on glassy carbon: an analysis of the effect of ultrasound, *J. Electroanal. Chem.* 523 (2002) 49–63.
- [32] E. Maisonhaute, C. Prado, P.C. White, R.G. Compton, Surface acoustic cavitation understood via nanosecond electrochemistry. Part III: Shear stress in ultrasonic cleaning, *Ultrason. Sonochem.* 9 (2002) 297–303.
- [33] D. Grujicic, B. Pesic, Iron nucleation mechanisms on vitreous carbon during electrodeposition from sulfate and chloride solutions, *Electrochim. Acta* 50 (2005) 4405–4418.
- [34] D.K. Owens, R.C. Wendt, Estimation of the Surface Free Energy of Polymers, *J. Appl. Polym. Sci.* 13 (1969) 1741–1747.
- [35] A.J. Bard, L.R. Faulkner, *Electrochemical methods: fundamentals and applications*, Wiley New York, 1980.
- [36] E.L. Cussler, *Diffusion Mass Transfer in Fluid Systems* 3rd edition, Cambridge University Press, 2009.
- [37] J.L. Trompette, H. Vergnes, Influence of base electrolytes on the electrodeposition of iron onto a silicon surface, *J. Phys. Chem. B* 110 (2006) 14779–14786.
- [38] E. Budevski, G. Staikov, W.J. Lorenz, *Electrochemical Phase Formation and growth: an introduction to the initial stages of metal deposition*, Wiley-VCH, 1996.
- [39] F. Marken, J.C. Eklund, R.G. Compton, Voltammetry in the presence of ultrasound: can ultrasound modify heterogeneous electron transfer kinetics? *J. Electroanal. Chem.* 395 (1995) 335–339.
- [40] N. Ibl, K. Schadeegg, Surface Roughness Effects in the Electrodeposition of Copper in the Limiting Current Range, *J. Electrochem. Soc.* 114 (1967) 54–58.
- [41] N. Ibl, P. Javet, F. Stahel, Note on the electrodeposits obtained at the limiting current, *Electrochim. Acta* 17 (1972) 733–739.
- [42] G. Orhan, G. Hapçı, Effect of electrolysis parameters on the morphologies of copper powder obtained in a rotating cylinder electrode cell, *Powder Technol.* 201 (2010) 57–63.
- [43] J. Israelachvili, *Intermolecular and surface forces*, 2nd edition, Academic P, 1999.
- [44] C. Chern, *Principles and Applications of Emulsion Polymerization*, John Wiley & Sons, 2008.
- [45] T.X. Phuoc, A comparative study of the photon pressure force, the photophoretic force, and the adhesion van der Waals force, *Opt. Commun.* 245 (2005) 27–35.
- [46] L.A. Girifalco, R.J. Good, A theory for the estimation of surface and interfacial energies. I. Derivation and application to interfacial tension, *J. Phys. Chem.* 61 (1957) 904–909.
- [47] M.E. Schrader, Wettability of clean metal surfaces, *J. Colloid Interface Sci.* 100 (1984) 372–380.
- [48] L. Vitos, A.V. Ruban, H.L. Skriver, J. Kollár, The surface energy of metals, *Surf. Sci.* 411 (1998) 186–202.